Comprehensive Monitoring of Gamma-ray Bright Blazars. I. Statistical Study of Optical, X-ray, and Gamma-ray Spectral Slopes

Karen E. Williamson[1], Svetlana G. Jorstad[1,2], Alan P. Marscher[1], Valeri M. Larionov[2,5,6], Paul S. Smith[3], Iván Agudo [4,1], Arkady A. Arkharov[5], Dmitry A. Blinov[7,2], Carolina Casadio[4], Natalia V. Efimova[2,5], José L. Gómez[4], Vladimir A. Hagen-Thorn[2,6], Manasvita Joshi[1], Tatiana S. Konstantinova[2], Evgenia N. Kopatskaya[2], Elena G. Larionova[2], Liudmilla V. Larionova[2], Michael P. Malmrose[1], Ian M. McHardy[8], Sol N. Molina[4], Daria A. Morozova[2], Gary D. Schmidt[9], Brian W. Taylor[1,10], and Ivan S. Troitsky[2]

kwilliam@bu.edu

ABSTRACT

We present γ-ray, X-ray, ultraviolet, optical, and near-infrared light curves of 33 γ-ray bright blazars over four years that we have been monitoring since 2008 August with multiple optical, ground-based telescopes and the *Swift* satellite, and augmented by data from the *Fermi Gamma-ray Space Telescope* and other publicly available data from *Swift*. The sample consists of 21 flat-spectrum radio quasars (FSRQs) and 12 BL Lac objects (BL Lacs). We identify quiescent and active states of the sources based on their γ-ray behavior. We derive γ-ray, X-ray, and optical spectral indices, α_γ, α_X, and α_o, respectively ($F_\nu \propto \nu^\alpha$), and construct spectral energy distributions (SEDs) during quiescent and active states. We analyze the relationships between different spectral indices, blazar classes, and activity states. We find (i) significantly steeper γ-ray spectra of FSRQs than for BL Lacs during quiescent states, but a flattening of the spectra for FSRQs during active states while the BL Lacs show no significant change; (ii) a small difference of α_X within each class between states, with BL Lac X-ray spectra significantly steeper than in FSRQs; (iii) a highly peaked distribution of X-ray spectral slopes of FSRQs at ~ -0.60, but a very broad distribution of α_X of BL Lacs during active states; (iv) flattening of the optical spectra of FSRQs during quiescent states, but no statistically significant change of α_o of BL Lacs between states; and (v) a positive correlation between optical and γ-ray spectral slopes of BL Lacs, with similar values of the slopes. We discuss the findings with respect to the relative prominence of different components of high-energy and optical emission as the flux state changes.

Subject headings: galaxies: active, galaxies: jets, quasars: general, BL Lacertae objects: general

[1]Institute for Astrophysical Research, Boston University, 725 Commonwealth Avenue, Boston, MA 02215

[2]Astronomical Institute, St. Petersburg State University, Universitetskij Pr. 28, Petrodvorets, 198504 St. Petersburg, Russia

[3]Steward Observatory, University of Arizona, Tucson, AZ 85721-0065

[4]Instituto de Astrofísica de Andalucía, CSIC, Apartado 3004, 18080, Granada, Spain

[5]Main (Pulkovo) Astronomical Observatory of RAS, Pulkovskoye shosse, 60, 196140, St. Petersburg, Russia

[6]Isaac Newton Institute of Chile, St. Petersburg Branch, St. Petersburg, Russia

[7]Department of Physics, University of Crete, 71003, Heraklion, Greece

[8]Department of Physics and Astronomy, University of Southampton, Southampton, SO17 1BJ, United Kingdom

[9]National Science Foundation, 4201 Wilson Ave., Arlington, VA, 22230 USA

[10]Lowell Observatory, Flagstaff, AZ 86001

1. Introduction

Blazars are active galactic nuclei characterized by ultra-luminous, broad-band, non-thermal radio to γ-ray continuum radiation, and by irregular, rapid flux variability across wavebands. They are divided into two classes, flat spectrum radio quasars (FSRQs) and BL Lac objects (BL Lacs). A primary method employed to probe our understanding of these objects is to study their spectral energy distributions (SEDs). Until recently, however, studies of blazar SEDs have been hindered by an insufficient number of simultaneous observations across the spectrum for a large enough sample of objects to allow a statistical analysis of their behavior in varying states of activity. A significant advance occurred with the launch of the *Fermi Gamma-ray Space Telescope*. With its sensitivity and its ability to scan the entire sky every three hours, the *Fermi* Large Area Telescope (LAT) (Atwood et al. 2009) provides continuous coverage of blazars in the γ-ray regime. One year prior to the onset of the science mission of *Fermi*, we began international, collaborative, multiwavelength monitoring of 33 blazars at radio to optical bands. These observations, combined with the γ-ray data from *Fermi* and the X-ray, ultraviolet (UV), and optical data from the *Swift* space observatory (Gehrels et al. 2004), as well as measurements with several ground-based instruments, provide a rich dataset to study the behavior of these objects. We focus on measurements across the electromagnetic spectrum, made within 24 hours of each other, at multiple epochs when the objects are in different γ-ray activity states.

Long-term monitoring of blazars reveals variability of emission best described by a "red noise" power spectrum, where the amplitude of variations is greater on longer time-scales (e.g., Do et al. 2009; Chatterjee et al. 2012). The light curves contain periods of relative quiescence interrupted by sometimes sudden, prominent outbursts with durations of weeks to several months in one or more energy bands, as well as more rapid lower-level fluctuations. These outbursts can vary dramatically in both time profile and amplitude. Critical to unraveling the physics of blazars is to study how the SED changes between such quiescent and active periods. Many studies have examined a small number of objects in an active state, sometimes contrasting activity at different flux levels (e.g., Raiteri et al. 2008a, 2012; Hayashida et al. 2012; Jorstad et al. 2013). Fewer (e.g., Raiteri et al. 2007, 2008a; Tagliaferri et al. 2008; Palma et al. 2011) have studied objects in a quiescent or low γ-ray state. With the increased sensitivity of instruments and the time coverage of *Fermi*, studies of larger samples are beginning to unveil trends in the behavior of blazars at different γ-ray activity states (e.g., Ghisellini et al. 2009; Abdo et al. 2010b). A statistical analysis of SEDs from optical to γ-ray wavelengths based on simultaneous observations at different activity states for a sample of blazars should, therefore, be instructive.

A distinctive characteristic of a blazar's SED is its two-peaked shape, with one maximum at infrared (IR) to X-ray frequencies and the other at γ-ray frequencies. The shape of the SED, combined with polarization characteristics, provides considerable evidence that the emission produced from radio to optical wavelengths is dominated by synchrotron radiation. If the accretion disk luminosity is important, it will be seen in the UV portion of the spectrum. Commonly seen in other classes of active galactic nuclei (AGNs), the "big blue bump" (BBB) is often less prominent, or even undetectable in blazars, owing to the strong, relativistically beamed non-thermal radiation. D'Elia et al. (2003) found that the non-thermal component of the optical/UV emission of FSRQs accounts for an average of $\sim 85\%$ of the total power. Only in about 9% of the objects they studied did the thermal component dominate. Signatures of the BBB in FSRQs include a decrease of the degree of polarization with frequency (e.g., Smith et al. 1986) and a redder color index at brighter flux states (e.g., Bregman et al. 1986; Raiteri et al. 2012). A number of observations have indicated that the accretion disk is less prominent in BL Lacs (e.g., Ghisellini et al. 2009; Giommi et al. 2012a). An alternative possibility for flatter-spectrum emission in the UV region of some blazars was suggested by Raiteri et al. (2005). Studying the spectrum of 0235+164, these authors see the signature of a second synchrotron component.

The higher-energy SED is consistent with inverse Compton (IC) scattering off photons either from inside the jet (synchrotron self-Compton mechanism, SSC) or external to the jet (external Compton mechanism, EC) by relativistic electrons in the jet (e.g., Marscher et al. 2010). Other mechanisms, e.g., proton synchrotron emission (Böttcher et al. 2013), might play a role as well. In IC models, we expect the spectral slope of high-energy emission to be similar to the slope of the synchrotron radiation emitted by the electrons responsible for scattering seed photons up to high energies.

The locations of radiative dissipation zones within the jet and the physical processes involved are still under debate. Polarization and timing of flares relative to changes in images of parsec-scale jets of blazars indicate that near-infrared (NIR) to optical synchrotron flares often take place near the end of the jet's acceleration zone (Jorstad et al. 2007; Marscher et al. 2008). Using Very Long Baseline Array (VLBA) images, Jorstad et al. (2012) conclude that enhanced γ-ray emission is produced downstream of the broad emission line clouds, while others (e.g., Tavecchio et al. 2010) argue for a sub-parsec origin, based on short timescales of γ-ray variability. The outbursts, which occur across the electromagnetic spectrum, can be caused by shock formations in the jet or other processes that increase the particle density, magnetic field strength, or seed photon field, change the magnetic field orientation, and/or enhance the Doppler boosting. The characteristics of the SED represented by spectral indices at different wavebands can provide insights into the interplay between different factors responsible for the outbursts, as well as between different emission components (e.g., the accretion disk and jet) and processes (synchrotron, inverse Compton, and thermal) during active and quiescent states. These insights will improve our understanding of the physics and location of energetic phenomena in blazars.

Here we statistically study how the spectral indices at γ-ray, X-ray, and optical frequencies change as the flux state varies, as well as whether the behavior depends on the type of blazar. We present over four years of data (from early 2008 to late 2012) in 13 frequency bands from NIR to γ-rays. From this compilation, we select epochs of quasi-simultaneous data at both active and quiescent states, compute spectral indices, and examine the trends and correlations between them. The sample of blazars and the data reduction are described in §2. In §3, we define *quiescent* and *active* states and describe the selection of epochs for our statistical analysis. We describe the computation of spectral indices in §4 and present the trends and correlations of those indices and in the relationships between them in §5. Using these statistical trends, we describe a "typical" quiescent and active BL Lac object and FSRQ in §6 and discuss the implications of our results for physical models. We summarize our findings in §7. An expanded version of this paper with a complete set of light curves and SEDs for all sources can be found at `www.bu.edu/blazars/VLBAproject.html`.

2. Observations and Data Reduction

2.1. The Sample

Since 2007, we have been collecting multi-waveband fluxes, polarization measurements, and radio images of blazars to provide the data for understanding the physics of the jets (see, e.g., Marscher 2012). This study includes 28 of the original 30 objects selected for the monitoring campaign, confirmed as γ-ray sources by EGRET (Energetic γ-Ray Experiment Telescope) on the *Compton Gamma Ray Observatory*, have an R-band brightness exceeding 18 mag (bright enough for optical polarization measurements at a $1-2$ meter class optical telescope without needing excessive amounts of telescope time), exceed 0.5 Jy at 43 GHz, and have a declination accessible to the collaboration's observatories ($>-30°$). Three additional BL Lacs (1055+018, 1308+326, and 1749+096) and two FSRQs (3C345 and 3C446) included in this analysis were among those added when they were detected as γ-ray sources by the *Fermi* LAT (Abdo et al. 2009).

Table 1 presents general information about these 33 blazars. Column 1 is an object reference number that will be used in plots to identify each source, column 2 is the object name as used in this writing, column 3 is an alternate, commonly used name, column 4 is the object's name as listed in the 2FGL catalog (Ackermann et al. 2011), column 5 gives the redshift as reported in the NASA/IPAC Extragalactic Database (NED)[1], and columns

[1] `http://nedwww.ipac.caltech.edu`

6 and 7 are the right ascension and declination of the object as retrieved by Simbad and reported in http://heasarc.gsfc.nasa.gov. From Ackermann et al. (2011), we include the object's optical classification and the SED classification in columns 8 and 9, respectively. Of the 33 blazars, 12 have optical classifications as BL Lacs and 21 as FSRQs. Of the 12 BL Lacs, 5 have an SED classification (Abdo et al. 2010c) of low synchrotron peak frequency (LSP, $\lesssim 10^{14}$ Hz), 6 as intermediate synchrotron peak frequency (ISP, between 10^{14} and 10^{15} Hz), and 1 as high synchrotron peak frequency (HSP, $\gtrsim 10^{15}$ Hz) blazar. All of the FSRQs have an SED classification of LSP.

2.2. Gamma-ray Data

The γ-ray data were obtained by the LAT on board the *Fermi Gamma Ray Space Telescope*. To construct the γ-ray light curves, we reduced the *Fermi* data using Pass 7 photon and spacecraft data, the V9r23p1 version of the Fermi Science Tools, and the instrument responses for the gal_2yearp7v6_v0 and iso_p7v6clean.txt diffuse source models. All of these are available on the *Fermi* website.[2] We modeled the γ-ray emission between 0.1 and 200 GeV from a given target and other point sources within a 15-degree radius of the target. Comprehensive reduction of the data was first performed with spectral models corresponding to those listed in the 2FGL catalog, typically with a seven-day bin size. However, because the power-law photon index in the 2FGL catalog was computed from the flux collected by *Fermi* over two years (Nolan et al. 2012), and because a typical blazar spends less than 5% of its time in a γ-ray active state (Abdo et al. 2010a), this index best represents the object in a quiescent state. To obtain a spectral index for each object while in an active state (to be defined in §3.1), we re-reduced the data during active states, typically with a 1-3 day bin size, using a simple power law model while allowing the photon index to vary. To obtain a spectral index during long periods of quiescence (defined in §3.1) when only upper limits were obtained with 7-day binning, we re-reduced the data using extended bin sizes.

[2]http://fermi.gsfc.nasa.gov/ssc/

2.3. X-Ray Data

The X-ray data, including the photon index and its uncertainty, were obtained at a photon energy range of 0.3−10 keV by the X-ray Telescope (XRT) (Burrows et al. 2005) on board the *Swift* satellite. We reduced the data using the standard HEAsoft package (version 6.11). The standard `xrtpipeline` task was used to calibrate and clean the events. We selected events with grades 0−12 in photon counting (PC) mode and 0−2 in windowed timing (WT) mode. An ancillary response file was created with PSF correction using the `xrtmkarf` task, and the the data were rebinned with the `grppha` task to ensure a minimum of 10 photons in every newly defined channel. We fit the spectra with the spectral analysis tool `xspec`, using a power-law model with minimum χ^2 value, and, except for 0235+164, fixing the hydrogen column density (N_H) according to the measurements of Dickey & Lockman (1990). For 0235+164, a value of N_H of 2.8×10^{21} cm^{-2} was used to include an intervening $z = 0.524$ absorber (Madejski et al. 1996; Ackermann et al. 2012). A Monte-Carlo method was used to test the goodness of fit.

The photon counts of the sources were checked for pileup. The threshold for pileup is 0.5 counts s^{-1} and 100 counts s^{-1} for PC mode and WT mode, respectively. Each event with pileup was individually re-examined to remove the center of the point-spread function (PSF), following the process outlined on the *Swift* website.[3] We created a new annular source region, determining the inner radius by modeling the PSF as a King function. None of the WT mode events exceeded the threshold for pileup.

2.4. Swift Optical and Ultraviolet Data

UV/Optical Telescope (UVOT) (Roming et al. 2005) data were reduced by using the standard HEAsoft package (version 6.11) and the calibration files released in 2011 July. For each object, we defined a selection region centered on the source with a standard radius of 5″, except for very faint objects (e.g., 0528+134, 0827+243), for which we chose a 3″ radius and performed aperture correction according to Poole et al. (2008). The back-

[3]http://www.swift.ac.uk/analysis/xrt/pileup.php.

Table 1
Sources Analyzed

Ref Num (1)	Object Name (2)	Alternate Name (3)	2FGL Catalog Name[a] (4)	z[b] (5)	R.A. 2000[c] (6)	Dec. 2000[c] (7)	Optical Class[a] (8)	SED Class[a] (9)
1	3C66A	0219+428	J0222.6+4302	0.444?	02 22 39.61	+43 02 07.8	BL Lac	ISP
2	0235+164		J0238.7+1637	0.940	02 38 38.93	+16 36 59.3	BL Lac	LSP
3	0336-019	CTA26	J0339.4-0144	0.852	03 39 30.94	-01 46 35.8	FSRQ	LSP
4	0420-014	OA129	J0423.2-0120	0.916	04 23 15.80	-01 20 33.1	FSRQ	LSP
5	0528+134		J0530.8+1333	2.060	05 30 56.42	+13 31 55.1	FSRQ	LSP
6	0716+714		J0721.9+7120	0.300[d]	07 21 53.45	+71 20 36.4	BL Lac	ISP
7	0735+178		J0738.0+1742	0.424	07 38 07.39	+17 42 19.0	BL Lac	LSP
8	0827+243	OJ248	J0830.5+2407	0.940	08 30 52.09	+24 10 59.8	FSRQ	LSP
9	0829+046		J0831.9+0429	0.174	08 31 48.88	+04 29 39.1	BL Lac	LSP
10	0836+710		J0841.6+7052	2.172	08 41 24.37	+70 53 42.2	FSRQ	LSP
11	OJ287	0851+202	J0854.8+2005	0.306	08 54 48.87	+20 06 30.6	BL Lac	ISP
12	0954+658		J0958.6+6533	0.368	09 58 47.25	+65 33 54.8	BL Lac	ISP
13	1055+018	4C+01.28	J1058.4+0133	0.890	10 58 29.61	+01 33 58.8	BL Lac	LSP
14	Mkn421	1101+384	J1104.4+3812	0.030	11 04 27.31	+38 12 31.8	BL Lac	HSP
15	1127-145		J1130.3-1448	1.184	11 30 07.05	-14 49 27.4	FSRQ	LSP
16	1156+295	4C+29.45	J1159.5+2914	0.724	11 59 31.83	+29 14 43.8	FSRQ	LSP
17	1219+285	WCom	J1221.4+2814	0.102	12 21 31.69	+28 13 58.5	BL Lac	ISP
18	1222+216	4C+21.35	J1224.9+2122	0.432	12 24 54.45	+21 22 46.5	FSRQ	LSP
19	3C273	1226+023	J1229.1+0202	0.158	12 29 06.70	+02 03 08.7	FSRQ	LSP
20	3C279	1253-055	J1256.1-0547	0.536	12 56 11.17	-05 47 21.5	FSRQ	LSP
21	1308+326		J1310.6+3222	0.996	13 10 28.66	+32 20 43.8	FSRQ	LSP
22	1406-076		J1408.8-0751	1.494	14 08 56.48	-07 52 26.7	FSRQ	LSP
23	1510-089		J1512.8-0906	0.360	15 12 50.53	-09 05 59.8	FSRQ	LSP
24	1611+343	DA406	J1613.4+3409	1.397	16 13 41.06	+34 12 47.9	FSRQ	LSP
25	1622-297		J1626.1-2948	0.815	16 26 06.02	-29 51 27.0	FSRQ	LSP
26	1633+382	4C+38.41	J1635.2+3810	1.814	16 35 15.49	+38 08 04.5	FSRQ	LSP
27	3C345	1641+399	J1642.9+3949	0.593	16 42 58.81	+39 48 37.0	FSRQ	LSP
28	1730-130	NRAO 530	J1733.1-1307	0.902	17 33 02.71	-13 04 49.5	FSRQ	LSP
29	1749+096	OT081	J1751.5+0938	0.322	17 51 32.82	+09 39 00.7	BL Lac	LSP
30	BL Lacertae	2200+420	J2202.8+4216	0.069	22 02 43.29	+42 16 40.0	BL Lac	ISP
31	3C446	2223-052	J2225.6-0454	1.404	22 25 47.26	-04 57 01.4	FSRQ	LSP
32	CTA102	2230+114	J2232.4+1143	1.037	22 32 36.42	+11 43 50.8	FSRQ	LSP
33	3C454.3	2251+158	J2253.9+1609	0.859	22 53 57.75	+16 08 53.6	FSRQ	LSP

[a]Ackermann et al. (2011).

[b]Information taken from the NASA/IPAC Extragalactic Database (http://nedwww.ipac.caltech.edu/).

[c]Simbad resolver as reported in http://heasarc.gsfc.nasa.gov.

[d]Danforth et al. (2013) set $0.2315 < z < 0.372$ (99.7%).

ground region was defined in a source-free region with a circular aperture of 20″. Unaligned exposures were individually aligned. All extensions within an image were summed with `uvotimsum` and processed with `uvotsource` using a sigma value of five. Only epochs with a summed exposure time exceeding 40 seconds were retained.

2.5. Ground-Based Optical and Near-Infrared Data

In addition to UVOT data, we used optical data from eight ground-based observatories. Table 2 provides the symbol we use to identify each observatory in light curves and SEDs (column 1), the identifying color of the observatory in light curves (column 2), the location of the observatory (column 3), the diameter of the telescope (column 4), and the wavebands of the data used in this study (column 5). References to the data reduction procedures are listed in the footnotes of the table.

2.6. Dereddening and Flux Conversion

For the UV observations, we dereddened the fluxes using the Fitzpatrick (1999) interstellar extinction curve with an R_v of 3.1 and A_λ values (Schlafly & Finkbeiner 2011) as retrieved from NED in 2012 November. Optical and NIR magnitudes were dereddened using the Schlafly & Finkbeiner (2011) values. Dereddening of 0235+164 is complicated by intervening sources of dust and optical emission. We followed the procedure of Raiteri et al. (2008b) to remove the additional flux from a foreground galaxy and applied the extinction values from Raiteri et al. (2005) and Ackermann et al. (2012). We converted the dereddened magnitudes to fluxes using the zero points and Pickles star spectra conversion factors from Poole et al. (2008) for *Swift* observations and Mead et al. (1990) for ground-based observations. For most objects in our sample, the host galaxy contribution is negligible in the UV. However, host galaxy contamination was subtracted for two nearby objects, BL Lacertae and Mkn 421. The host contribution in the UV is expected to be negligible for these two sources. We used the R-Band host galaxy flux values derived by Nilsson et al. (2007) and average effective colors for elliptical galaxies determined by Mannucci et al. (2001). Converting these values as above, we obtained the dereddened host galaxy flux values, reported in Table 3. We subtracted these constant values from the dereddened measured flux.

2.7. Calibration of Near-Infrared through Ultraviolet Spectra

To determine if any observatory has magnitudes for a band that are consistently higher or lower than other observatories, we examined all measurements for all objects, selecting sets of measurements when a minimum of two observatories observed an object in the same band within the same day. We restricted the observations to days when the source was not active in any NIR through U bands. If an observatory had multiple observations within a given day, we computed a weighted mean for each such day and band. We then analyzed the differences between the fluxes from different observatories for a given band based on different epochs and sources.

Overall, no systematic discrepancies appear to be present in any band for any observatory, with the exception of the SMARTS K band; hence, these data are used with caution. All light curves were checked for outliers, which were deleted in the final analysis.

3. Quiescent and Active Epochs

3.1. Properties of Quiescent and Active States

Our monitoring program has resulted in a sufficient number of quasi-simultaneous measurements of each object at different frequencies to compute and compare the spectral indices when objects were in an active versus a quiescent state. Barring a few definitions of "bright" or "flares" (see, e.g., Abdo et al. 2010a; Nalewajko 2013), there is no standard definition for "quiescent" and "active." We define these states based on the weighted mean flux, $\langle F_\nu \rangle$, and its weighted standard deviation,

$$\sigma_{w_\nu} = \sqrt{\frac{\sum_{i=1}^{N} w_i (x_i - \langle F_\nu \rangle)^2}{\frac{(N-1)\sum_{i=1}^{N} w_i}{N}}}, \qquad (1)$$

where x_i is a measurement with uncertainty σ_i, $w_i = 1/\sigma_i^2$ is the weight of the individual measurement, and N is the number of observations

Table 2

List of Observatories Providing Measurements for this Study

Symbol			Telescope	
Shape	Color (Light curves)	Observatory (Telescope or Monitoring Program) and Location	Diameter	Wavebands
Space-based				
◇	black	*Fermi* Gamma Ray Space Telescope (LAT)		Gamma-ray (0.1 GeV − 300 GeV)
△	black	*Swift* Space Satellite (XRT)		X-ray (0.3 − 10 keV)
△, ◖, ⊓	black, green, orange	*Swift* Space Satellite (UVOT)		*UVW1, UVM2, UVW2*
△	black	*Swift* Space Satellite (UVOT)		*U, B, V*
Ground-based				
×	indigo	Lowell Observatory (Perkins Telescope), Flagstaff, Arizona[a]	1.83 m	*B, V, R, I*
◁	light blue	Crimean Astrophysical Observatory (AZT-8), Nauchnij, Ukraine[b]	0.70 m	*B, V, R, I*
▽	green	Observatorio del Roque de los Muchachos (Liverpool Telescope), La Palma, Spain[a]	2.00 m	*R*
◗	dark orange	Calar Alto Observatory (MAPCAT), Andalucía, Spain[c]	2.20 m	*R*
□	blue	Cerro Tololo Inter-American Observatory (SMARTS), Cerro Tololo, Chile[d]	0.90 − 1.50 m	*B, V, R, J, K*
▷	red	St. Petersburg University (LX-200), St. Petersburg, Russia[b]	0.40 m	*B, V, R, I*
○	yellow	Steward Observatory (Kuiper and Bok Telescopes), Mt. Bigelow and Kitt Peak, Arizona[e]	1.54, 2.30 m	*V*
⧗	red	Istituto Nazionale di Astrofisica (AZT-24), Campo Imperatore, Italy[f]	1.10 m	*J, H, K*

[a]Data reduction is performed with the ESO software package MIDAS; refer to Jorstad et al. (2010).

[b]Data reduction details provided in Larionov et al. (2008).

[c]Monitoring AGN with Polarimetry at the Calar Alto Telescopes (MAPCAT); data reduction details provided in Agudo et al. (2012).

[d]The Small and Moderate Aperture Research Telescope System (SMARTS) daily monitoring program; refer to `http://www.astro.yale.edu/smarts/`.

[e]Data reduction details provided in Smith et al. (2009).

[f]AZT-24 observations are made within an agreement between Pulkovo Astronomical Observatory, Rome Astronomical Observatory, and Collurania-Teramo Observatory. Data reduction details provided in Hagen-Thorn et al. (2008).

TABLE 3
HOST GALAXY CONTAMINATING FLUX

Object and Measurement Source (1)	Uncorrected R-Band Flux[a] (uncertainty) (2)	Dereddened Host Galaxy Flux [mJy] U (3)	B (4)	V (5)	R (6)	I (7)	J (8)	H (9)	K (10)
BL Lacertae									
Ground-based	1.35 (0.03)	0.23	0.84	1.79	2.61	3.85	7.38	9.08	6.84
Swift	1.13 (0.03)	0.19	0.70	1.50					
Mkn 421									
Ground-based	7.8 (0.4)	0.7	2.6	5.5	8.0	11.9			
Swift	6.2 (0.4)	0.6	2.1	4.4					

[a]Nilsson et al. (2007).

NOTE.—Ground-based values are for a typical aperture radius of 7 arcsec, and for Swift, the typical 5 arcsec radius.

of the source within a given energy band ν. All measurements from all observatories, subject to restrictions stated in Section 2.7 and with a self-imposed minimum of ten measurements within a band, were used to compute these values. We set as an upper limit to a *quiescent* flux level $\langle F_\nu \rangle$, and as a lower limit to an *active* flux level $\langle F_\nu \rangle + 1\sigma_{w_\nu}$. Between these levels, we consider the source to be in a transitional state. Additionally, we further define a *flaring* flux level to be when the flux exceeds $\langle F_\nu \rangle + 3\sigma_{w_\nu}$. For *Fermi* data, we include upper limits in the computation of $\langle F_\gamma \rangle$, replacing both the flux and its error with the value of the upper limit. Table 4 presents $\langle F_\nu \rangle$, its weighted standard deviation, and the number of data points used in its computation for each of the selected frequency bands for each object.

We restrict our analysis to epochs when γ-ray emission was in a sustained period of either quiescence or active flux levels. A flaring flux level is, by definition, part of an active state. Based on our typical 7-day binning of γ-ray data, we require a quiescent period to extend a minimum of 21 consecutive days, with upper limits considered quiescent, and an active period to extend a minimum of 14 consecutive days. As an example, for 7-day binning of *Fermi* data, a minimum of two consecutive data points at least $1\sigma_{w_\gamma}$ above $\langle F_\gamma \rangle$ are required before we consider the source to be in an active state. Active γ-ray periods thus determined initially have been reevaluated using *Fermi* light curves computed with the photon index allowed to vary. A minor exception is made for the active epochs of 1749+096. We allow two active periods to include epochs when the γ-ray measurement fell marginally below, and well within the uncertainties, of the lower limit for active periods. To evaluate the state of a source at the other bands during a given γ-ray state, no minimum duration is imposed.

Table 5 presents a summary of the γ-ray periods of quiescence for BL Lacs and FSRQs. The columns of Table 5 are as follows: 1 - the object name, 2 - the number of quiescent periods, 3 - the total number of days during which the object was in a quiescent period (note that this excludes any days for which the object had a low flux value but for less than an uninterrupted 21-day period), and 4−6 - the number of days in the longest uninterrupted period of quiescence and the dates of the beginning and end of the longest period, respectively. Similarly, Table 6 presents a summary of the γ-ray active periods (all active periods are identified from the data computed with a fixed photon index): column 1 is the object name, column 2 is the number of active periods identified for the object, column 3 is the number of active periods that have a flux value considered to be in a flaring state, and column 4 is the total number of days during which the object was in an active period. Columns 5−7 list the number of days in the longest uninterrupted active period and the dates of the beginning and end of the longest active period, respectively. Columns 8−10 give the maximum flux observed, its uncertainty, and the central date of the bin, respectively. The spectral index at the time of measurement of the maximum flux is listed in column 11. If the maximum flux was computed using the fixed photon index in the 2FGL catalog, an "F" is inserted in column 12; otherwise, if the photon index was allowed to vary, a "V" is inserted in column 12 (see Section 4). Columns 13 and 14 present the ratio of the maximum flux to $\langle F_\gamma \rangle$ and the uncertainty that characterizes an amplitude of γ-ray variability.

To identify trends based on the class of objects, we generate a series of plots using the values in Tables 5 and 6. Histograms of the percentage of time that each source was in a quiescent or active period are presented in Figure 1. Note that measurements in a transitory state or in isolated quiescent/active states are included in the total time. BL Lacs and FSRQs show similar behavior. BL Lacs spend an average of 55 ± 20% of their time in quiescent periods, while FSRQs spend 65 ± 15% of their time in quiescent periods. Time spent in active periods for BL Lacs is 9 ± 4% and for FSRQs, 10 ± 8%. Both averaged 5 ± 3 active periods over the 4.2 years of Fermi measurements included in this study, and BL Lacs averaged 12 ± 4 quiescent periods and FSRQs 11 ± 5.

Histograms of the longest uninterrupted quiescent and active periods for each of the sources are displayed in Figure 2. Time is in the host galaxy frame, adjusted for redshift. We checked the ends of the light curves for the longest uninterrupted periods. Four of our objects (0827+243, 0954+658, 1222+216, and 1622-297), were within their longest uninterrupted quiescent period at the start of the *Fermi* mission and the longest uninterrupted active period was in progress for 1308+326. Additionally, 4 of our objects (3C279, 3C345, 3C446, and 3C454.3) were within their longest uninterrupted quiescent period at the end of the monitoring period for this paper. Thus, for these objects, our longest uninterrupted periods

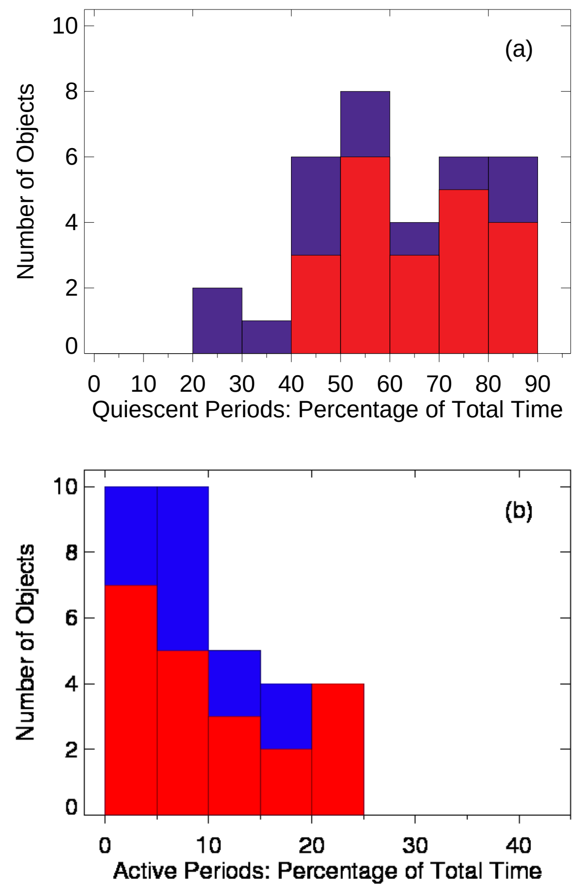

Fig. 1.—: Histograms of the percent of time that sources were in a γ-ray quiescent (a) or active (b) period. (See text for definitions of periods.) FSRQs are red-filled and BL Lac objects, blue-filled.

represent lower limits. No obvious trends exist for either subclass while in a quiescent state, with both having wide dispersions. The longest uninterrupted quiescent period for most BL Lacs ran from 68 days (0735+178) to 232 days (1055+018), but 0235+164 and 0829+046 had 599 and 543 days, respectively. All but four FSRQs (3C273, 1611+343, 0827+243, and 1127-145) had fewer than 265 days in their longest uninterrupted quiescent period, with the length generally equally dispersed from a minimum of 78 days (3C446). The longest uninterrupted active periods were also highly dispersed for both subclasses, with BL Lac objects generally having a longer uninterrupted period (ranging from 15 to 95 days and averaging 43 ± 27 days) than FSRQs (ranging from 6 to 73

Table 4

Weighted Mean Flux and Weighted Standard Deviations (Part 1 of 3): Gamma-ray through UVW1 Bands

Object	*Fermi* γ-ray [phot cm^{-2} s^{-1}]			*Swift* XRT [erg cm^{-2} s^{-1}]			*Swift UVW2* [mJy]			*Swift UVM2* [mJy]			*Swift UVW1* [mJy]		
Name	$\langle F_{\gamma} \rangle$	1-$\sigma_{w_{\gamma}}$	# Items	$\langle F_X \rangle$	1-σ_{w_X}	# Items	$\langle F_{W2} \rangle$	1-$\sigma_{w_{W2}}$	# Items	$\langle F_{M2} \rangle$	1-$\sigma_{w_{M2}}$	# Items	$\langle F_{W1} \rangle$	1-$\sigma_{w_{W1}}$	# Items
(1)	(2)	(3)	(4)	(5)	(6)	(7)	(8)	(9)	(10)	(11)	(12)	(13)	(14)	(15)	(16)
3C66A	1.25E-07	6.99E-08	213	4.09E-12	2.15E-12	19	2.313	0.832	16	2.368	0.883	13	3.549	1.320	15
0235+164	1.88E-07	2.74E-07	206	2.28E-12	1.96E-12	91	0.186	0.277	99	0.250	0.384	95	0.292	0.460	99
0336-019	1.23E-07	8.20E-08	213			5			7			6			7
0420-014	1.33E-07	6.81E-08	213	2.62E-12	6.87E-13	16	0.136	0.038	12	0.203	0.078	12	0.243	0.080	13
0528+134	1.10E-07	8.28E-08	216	2.36E-12	1.41E-12	73	0.476	0.177	10			9	0.328	0.195	14
0716+714	2.17E-07	1.38E-07	501	7.60E-12	4.31E-12	103	3.975	2.034	76	4.316	2.107	72	6.080	3.015	83
0735+178	7.08E-08	3.02E-08	212	8.12E-13	3.75E-13	14	0.285	0.127	11	0.339	0.137	10			9
0827+243	1.51E-07	1.30E-07	228	2.76E-12	1.85E-12	63	0.241	0.045	44	0.280	0.052	50	0.376	0.071	47
0829+046	6.41E-08	3.78E-08	209	1.13E-12	5.74E-13	16			7			7			7
0836+710	1.58E-07	1.42E-07	208	1.64E-11	4.38E-12	28	0.057	0.008	12	0.077	0.009	11	0.172	0.022	13
OJ287	1.05E-07	8.11E-08	209	4.81E-12	2.31E-12	127	1.088	0.464	100	1.170	0.504	90	1.773	0.757	119
0954+658	6.86E-08	4.71E-08	209	2.15E-12	1.17E-12	14	0.097	0.046	11			9	0.164	0.067	14
1055+018	1.17E-07	6.69E-08	214	2.74E-12	9.51E-13	13			8			5			5
Mkn421	1.79E-07	7.29E-08	219	6.09E-10	1.72E-10	288	11.771	3.668	415	11.924	3.817	402	15.449	5.086	388
1127-145	1.03E-07	6.01E-08	219	5.50E-12	1.74E-12	23	0.217	0.058	19	0.274	0.069	19	0.434	0.100	20
1156+295	1.43E-07	1.04E-07	214	1.34E-12	4.73E-13	21			8			8	0.454	0.392	10
1219+285	6.03E-08	2.62E-08	219	2.14E-12	1.97E-12	74	1.054	0.510	70	1.119	0.540	68	1.660	0.747	75
1222+216	2.02E-07	3.37E-07	213	3.21E-12	7.65E-13	66	1.671	0.417	38	1.554	0.380	41	1.983	0.502	41
3C273	3.14E-07	3.34E-07	214	1.20E-10	4.73E-11	148	24.924	3.002	29	24.202	2.688	23	30.848	2.869	27
3C279	3.43E-07	2.71E-07	208	1.03E-11	2.85E-12	284	0.353	0.454	142	0.400	0.512	136	0.643	0.739	170
1308+326	7.38E-08	3.64E-08	219	1.43E-12	9.03E-13	14	0.078	0.055	10	0.120	0.064	11			7
1406-076	8.50E-08	4.02E-08	219	7.14E-13	1.75E-13	20	0.007	0.003	42	0.015	0.007	42	0.036	0.014	46
1510-089	6.11E-07	6.29E-07	214	6.78E-12	1.85E-12	157	0.537	0.244	154	0.615	0.242	141	0.731	0.335	153
1611+343	2.02E-08	1.92E-08	219			7			4			4			6
1622-297	9.98E-08	5.61E-08	156	2.23E-12	9.47E-13	39	0.256	0.060	43	0.302	0.092	41	0.282	0.108	47
1633+382	2.44E-07	1.87E-07	216	2.29E-12	1.59E-12	72	0.022	0.009	54	0.044	0.018	59	0.160	0.066	60
3C345	1.26E-07	6.56E-08	222	4.76E-12	1.05E-12	27	0.234	0.079	21	0.241	0.090	19	0.327	0.121	23
1730-130	1.82E-07	1.25E-07	213	1.65E-12	6.61E-13	46	0.114	0.045	37	0.182	0.063	25	0.197	0.084	48
1749+096	8.39E-08	5.17E-08	233	4.17E-12	3.05E-12	25	0.694	0.994	11	0.548	0.843	11	1.104	1.642	13
BL Lacertae	2.40E-07	1.63E-07	268	1.05E-11	6.78E-12	196	1.117	0.755	182	1.443	1.015	175	2.052	1.334	189
3C446	7.87E-08	4.33E-08	225			9			2			3			2
CTA102	2.05E-07	2.16E-07	324	4.43E-12	2.44E-12	53	0.437	0.306	36	0.514	0.351	32	0.692	0.493	39
3C454.3	7.79E-07	1.58E-06	1214	3.41E-11	3.31E-11	331	0.987	0.465	255	1.222	0.573	251	1.682	0.865	280

Table 4

Weighted Mean Flux and Weighted Standard Deviations (Part 2 of 3): U - R Bands

Object Name	U-BAND [mJy]			B-BAND [mJy]			V-BAND [mJy]			R-BAND [mJy]		
	$\langle F_U \rangle$	1-σ_{w_U}	# Items	$\langle F_B \rangle$	1-σ_{w_B}	# Items	$\langle F_V \rangle$	1-σ_{w_V}	# Items	$\langle F_R \rangle$	1-σ_{w_R}	# Items
(1)	(2)	(3)	(4)	(5)	(6)	(7)	(8)	(9)	(10)	(11)	(12)	(13)
3C66A	4.492	1.733	15	5.525	2.170	412	7.090	2.783	590	6.795	2.941	786
0235+164	0.507	0.817	82	0.207	0.312	427	0.497	0.750	690	0.523	0.814	1249
0336-019			6	0.412	0.189	13	0.377	0.129	29	0.600	0.242	211
0420-014	0.247	0.072	10	0.441	0.330	78	0.579	0.343	154	0.686	0.653	365
0528+134	0.262	0.122	41	0.334	0.093	173	0.334	0.127	203	0.296	0.049	356
0716+714	8.111	3.735	79	10.626	4.916	960	14.759	6.199	1112	21.304	9.848	1908
0735+178	0.658	0.229	10	0.865	0.240	21	1.218	0.402	94	1.350	0.346	240
0827+243	0.415	0.115	45	0.460	0.088	42	0.488	0.105	192	0.481	0.080	276
0829+046			7	0.708	0.373	29	1.491	0.754	46	1.726	0.672	149
0836+710	0.474	0.039	11	0.582	0.050	67	0.633	0.060	104	0.677	0.094	313
OJ287	2.400	0.960	110	3.257	1.381	826	4.669	1.905	1051	5.258	2.260	1215
0954+658	0.261	0.099	12	0.491	0.295	182	0.689	0.385	229	0.950	0.552	933
1055+018			7	0.355	0.165	11	0.657	0.368	13	0.756	0.238	100
Mkn421	8.914	3.656	10	18.382	6.930	94	19.096	7.779	304	24.475	12.253	263
1127-145			4	0.599	0.153	31			9	0.781	0.076	112
1156+295	0.430	0.441	13	0.824	0.932	118	0.397	0.483	94	0.582	0.751	565
1219+285	2.102	0.887	73	2.662	1.001	170	3.749	1.394	334	4.729	1.369	304
1222+216	1.927	0.448	48	2.074	0.494	50	2.162	0.596	234	2.406	0.853	228
3C273			4	27.088	1.877	423	31.260	2.166	574	31.750	2.366	248
3C279	0.916	1.063	171	0.779	1.040	636	1.632	2.093	817	0.928	0.857	914
1308+326			7	0.143	0.115	20	0.174	0.158	22	0.264	0.147	173
1406-076	0.076	0.024	47	0.100	0.033	230	0.119	0.036	222	0.144	0.046	286
1510-089	0.963	0.431	147	1.096	0.522	660	1.236	0.759	850	1.347	0.642	1129
1611+343			6	0.373	0.028	50	0.358	0.057	54	0.433	0.055	258
1622-297	0.333	0.067	42	0.441	0.100	223	0.756	0.222	232	0.409	0.150	239
1633+382	0.332	0.142	56	0.439	0.228	241	0.395	0.235	429	0.470	0.211	717
3C345	0.322	0.162	22	0.474	0.332	220	0.540	0.367	287	0.450	0.207	699
1730-130	0.183	0.083	46	0.331	0.126	272	0.473	0.209	271	0.874	0.470	368
1749+096	2.531	2.991	11	2.798	3.591	55	3.213	4.443	79	0.907	0.490	459
BL Lacertae	3.144	2.065	184	4.844	3.021	818	7.710	4.571	1152	13.385	7.517	1318
3C446			5	0.030	0.053	13	0.152	0.035	25	0.216	0.079	188
CTA102	0.806	0.777	33	0.752	0.890	175	1.162	1.446	286	1.046	1.344	794
3C454.3	2.144	1.406	225	2.549	1.728	988	4.061	2.780	1304	3.221	3.090	1578

Table 4
Weighted Mean Flux and Weighted Standard Deviations (Part 3 of 3): I - K Bands

Object Name	I-BAND [mJy] $\langle F_I \rangle$	$1\text{-}\sigma_{w_I}$	# Items	J-BAND [mJy] $\langle F_J \rangle$	$1\text{-}\sigma_{w_J}$	# Items	H-BAND [mJy] $\langle F_H \rangle$	$1\text{-}\sigma_{w_H}$	# Items	K-BAND [mJy] $\langle F_K \rangle$	$1\text{-}\sigma_{w_K}$	# Items
(1)	(2)	(3)	(4)	(5)	(6)	(7)	(8)	(9)	(10)	(11)	(12)	(13)
3C66A	9.323	3.788	498	12.355	4.022	245	18.191	5.699	238	24.548	7.169	252
0235+164	0.933	2.219	469	1.835	2.465	646	2.530	2.837	376	5.122	6.002	547
0336-019	0.773	0.323	33									
0420-014	1.456	1.238	112	1.850	0.933	55	2.833	1.632	55	2.821	2.430	55
0528+134	0.312	0.037	16	0.627	0.303	233	0.952	0.691	36	1.201	0.873	36
0716+714	26.156	12.430	990	22.779	8.237	346	45.092	13.925	137	57.176	21.710	134
0735+178	2.121	0.546	75	3.550	0.489	19	5.131	0.630	16	6.830	0.673	16
0827+243	0.496	0.146	36	0.602	0.119	18	0.635	0.170	15	0.807	0.302	15
0829+046	2.315	0.926	45	3.963	1.110	20	5.867	1.724	16	8.277	1.849	16
0836+710	0.770	0.048	22	1.046	0.483	35	1.106	0.612	23	1.502	1.016	21
OJ287	7.363	3.002	460	13.000	5.704	407	19.070	6.749	62	35.597	17.029	313
0954+658	1.345	0.538	98	2.473	1.193	60	3.917	1.761	54	5.756	3.064	49
1055+018			9									
Mkn421	32.674	7.614	11									
1127-145			5	0.568	0.126	31						9
1156+295	1.954	1.868	181	1.288	0.797	33	2.176	1.339	23	4.115	2.980	16
1219+285	5.861	1.635	109	10.653	1.798	29	15.241	2.342	27	17.913	2.886	23
1222+216			9									
3C273	40.046	2.983	214	40.485	2.299	310	54.576	3.834	15	96.516	3.114	16
3C279	1.801	1.276	164	2.721	2.646	416	3.693	2.067	37	8.811	9.013	362
1308+326	0.206	0.098	31									
1406-076			4	0.272	0.146	181				0.379	0.144	45
1510-089	1.879	0.938	250	2.393	1.676	444	3.323	1.101	76	8.011	6.008	382
1611+343	0.520	0.068	57	0.418	0.062	26	0.631	0.061	25	0.586	0.086	24
1622-297			1	0.887	0.430	189				1.669	1.146	182
1633+382	0.707	0.521	261	0.656	0.211	62	0.923	0.338	56	1.292	0.573	49
3C345	1.008	0.806	296	1.312	0.461	67	2.249	0.768	64	3.372	1.233	63
1730-130			4	1.331	0.523	242				3.102	1.635	213
1749+096	2.275	1.197	97			8						
BL Lacertae	18.983	8.823	750	47.059	10.521	62	71.696	16.745	58	92.027	21.234	59
3C446			8	0.378	0.096	53						2
CTA102	0.795	0.850	176	0.915	0.233	26	0.929	0.285	66	1.372	0.638	63
3C454.3	5.153	4.962	448	4.053	4.680	574	2.924	3.419	141	9.302	12.282	506

Table 5
Gamma-Ray Periods of Quiescence

Object Name (1)	Number of Periods (2)	Total Days in All Periods (3)	Longest Quiescent Period No. of Days (4)	Start Date (5)	End Date (6)
3C66A	11	517	133	5931.55	6064.55
0235+164	3	1260	1162	4958.52	6120.55
0716+714	10	431	97	4810.50	4907.52
0735+178	17	701	97	5413.55	5511.51
0829+046	8	889	637	5504.51	6141.54
OJ287	14	1051	288	4810.50	5098.54
0954+658	11	1506	267	4684.50	4951.54
1055+018	10	854	439	5022.54	5462.51
Mkn421	10	433	84	4858.16	4942.16
1219+285	20	715	195	5638.53	5833.53
1749+096	15	1216	175	5194.16	5369.16
BL Lacertae	12	723	189	5439.16	5628.16
FSRQs					
0336-019	10	869	491	4691.50	5182.51
0420-014	11	784	370	5344.55	5714.55
0528+134	13	1247	441	4880.50	5321.50
0827+243	5	1399	780	4684.50	5464.50
0836+710	7	1072	419	4895.56	5315.52
1127-145	2	1063	1042	5035.54	6078.53
1156+295	17	805	168	5595.51	5763.53
1222+216	11	715	253	4684.50	4937.52
3C273	12	792	378	5669.50	6047.50
3C279	6	650	350	5845.00	6195.00
1308+326	12	1080	336	5434.51	5770.53
1406-076	19	1157	210	5980.53	6190.53
1510-089	16	762	112	6050.53	6162.53
1611+343	4	1213	940	4683.16	5623.53
1622-297	9	884	401	4683.16	5084.54
1633+382	8	770	238	5860.50	6098.50
3C345	13	1167	399	5791.53	6190.53
1730-130	12	1251	476	4790.52	5266.54
3C446	19	1260	187	6062.16	6249.16
CTA102	12	1064	490	4963.16	5453.16
3C454.3	3	614	477	5708.16	6185.16

Note.—Time has not been adjusted for redshift.

— If two or more quiescent periods have the same longest duration, only the first is shown.

Table 6
Gamma-Ray Active Periods

Object Name (1)	Number of Periods (2)	Number Flaring Periods (3)	Total Days in All Periods (4)	Longest Active Period: No. of Days (5)	Longest Active Period: Start Date (6)	Longest Active Period: End Date (7)	Overall Highest Flux Measured: $\langle F_{max} \rangle$ (8)	Overall Highest Flux Measured: 1-σ (9)	Overall Highest Flux Measured: Date (10)	Spectral Index (11)	Source (12)	$\langle F_{max} \rangle$ / $\langle F_{\gamma} \rangle$ (13)	1-σ (14)
BL Lacs													
3C66A	10	2	238	70	4916.52	4986.52	7.43E-07	6.54E-08	4969.02	-0.85	F	6.0	3.4
0235+164	1	1	84	84	4691.50	4775.50	1.39E-06	1.27E-07	4728.00	-0.96	V	7.4	10.9
0716+714	6	3	105	21	6101.50	6122.50	2.18E-06	1.66E-07	5857.00	-0.91	V	10.0	6.4
0735+178	5	3	133	77	6085.55	6162.55	2.50E-07	4.44E-08	6138.05	-1.05	F	3.5	1.6
0829+046	5	2	119	42	5182.51	5224.51	4.43E-07	7.93E-08	5130.04	-1.09	V	6.9	4.3
OJ287	4	3	147	84	5819.54	5903.54	7.40E-07	8.81E-08	5872.04	-1.14	V	7.1	5.5
0954+658	3	3	49	21	5665.53	5686.53	3.02E-07	4.40E-08	5641.03	-1.42	F	4.4	3.1
1055+018	6	3	161	42	5623.53	5665.53	5.11E-07	1.54E-07	5648.01	-1.33	V	4.4	2.8
Mkn421	5	1	168	98	6099.53	6197.53	8.45E-07	6.53E-08	6124.03	-0.75	V	4.7	2.0
1219+285	3	1	63	28	4683.16	4711.16	1.88E-07	4.08E-08	4686.66	-1.02	F	3.1	1.5
1749+096	4	3	63	21	4683.16	4704.16	3.79E-07	5.41E-08	4686.66	-1.10	F	4.5	2.9
BL Lacertae	9	5	247	91	5691.16	5782.16	9.89E-07	7.41E-08	5708.66	-1.11	F	4.1	2.8
FSRQs													
0336-019	8	4	133	21	5532.50	5553.50	4.37E-07	6.96E-08	5550.00	-1.48	F	3.6	2.4
0420-014	7	1	168	56	5175.51	5231.51	4.92E-07	5.70E-08	5221.01	-1.30	F	3.7	1.9
0528+134	3	2	49	21	5805.55	5826.55	5.71E-07	7.19E-08	4723.00	-1.55	V	5.2	4.0
0827+243	2	2	119	77	6183.54	6260.54	7.11E-07	8.34E-08	6285.04	-1.30	V	4.7	4.1
0836+710	3	2	91	42	5894.01	5936.01	1.61E-06	1.32E-07	5870.05	-1.61	V	10.2	9.2
1127-145	2	1	63	35	4809.16	4844.16	2.99E-07	5.90E-08	4777.66	-1.61	V	2.9	1.8
1156+295	4	3	189	84	5420.51	5504.51	9.55E-07	7.31E-08	5431.01	-1.13	V	6.7	4.9
1222+216	9	6	350	105	5343.55	5448.55	5.82E-06	1.78E-07	5368.01	-1.08	V	28.8	48.0
3C273	8	4	273	84	5049.50	5133.50	5.30E-06	3.94E-07	5094.00	-1.40	V	16.9	18.0
3C279	9	4	287	63	4839.56	4902.56	1.91E-06	7.74E-08	4800.00	-1.20	V	5.6	4.4
1308+326	4	3	84	42	4683.16	4725.16	3.59E-07	4.16E-08	4714.66	-1.10	F	4.9	2.5
1406-076	4	1	56	14	4802.16	4816.16	2.08E-07	5.85E-08	5424.01	-1.43	F	2.5	1.4
1510-089	8	6	315	84	4951.54	5035.54	6.37E-06	2.01E-07	5872.03	-1.29	F	10.4	10.7
1611+343	0	0	0										
1622-297	2	0	28	14	5294.51	5308.51	2.39E-07	7.62E-08	5368.01	-1.34	F	2.4	1.6
1633+382	10	3	357	91	5678.50	5769.50	1.50E-06	1.08E-07	6193.00	-1.25	F	6.2	4.7
3C345	3	2	91	42	4951.54	4993.54	4.32E-07	9.28E-08	4976.04	-1.45	V	3.4	1.9
1730-130	2	1	49	35	5490.50	5525.50	9.15E-07	7.37E-08	5501.05	-0.97	V	5.0	3.5
3C446	1	0	21	21	4970.16	4991.16	1.64E-07	5.04E-08	4987.66	-1.44	F	2.1	1.3
CTA102	7	4	205	84	6178.53	6262.53	4.11E-06	1.95E-07	6194.03	-1.01	V	20.1	21.2
3C454.3	6	5	307	110	5480.16	5590.16	4.16E-05	4.86E-07	5522.04	-1.26	V	53.4	108.0

Note.—All flux values are in photon cm^{-2} s^{-1}. Time is in the observer's frame, not adjusted for redshift.
— If two or more active periods have the same longest duration, only the first is shown.

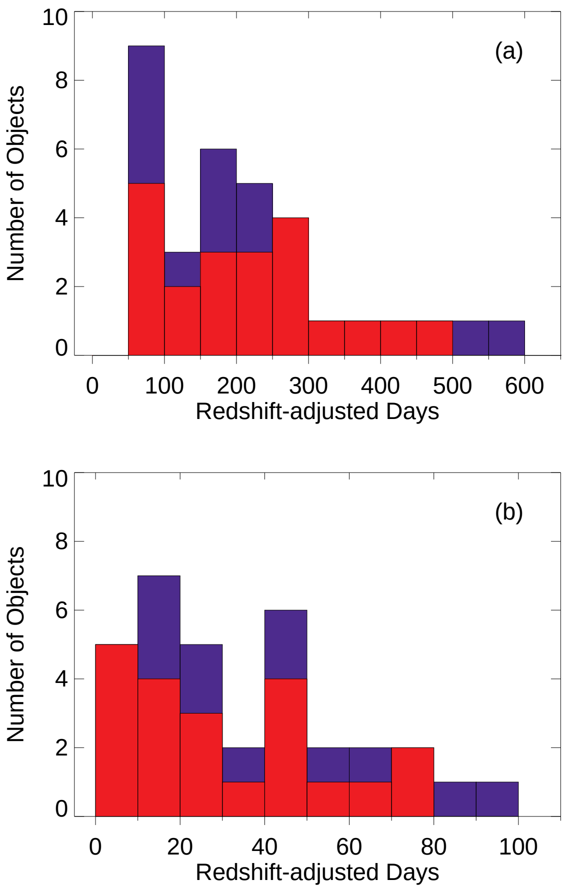

Fig. 2.—: Histograms of the durations of the longest uninterrupted periods of γ-ray (a) quiescent or (b) active activity, adjusted for redshift. FSRQs are red-filled and BL Lacs, blue-filled.

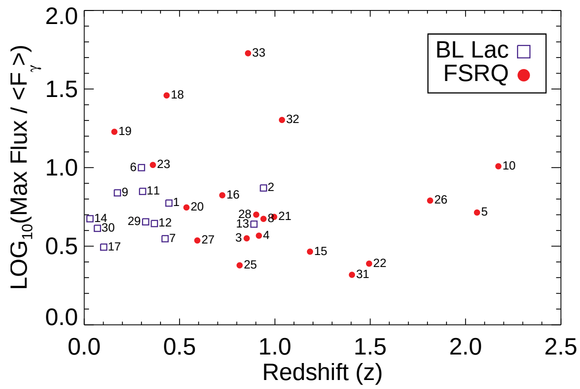

Fig. 3.—: Maximum amplitude of γ-ray variations achieved by each object (values listed in Table 6) vs. redshift. The labels refer to the object reference number (see Table 1). The highest amplitudes correspond to 3C454.3 (#33), 1222+216 (#18), CTA102 (#32), and 3C273 (#19).

days and averaging 30 $\pm$ 23 days) when converted to the respective galaxies' restframes.

We plot the normalized amplitude of flux variations vs. redshift in Figure 3. Noticeable is the lack of BL Lacs displaying large amplitudes. The average normalized amplitudes are 5.5$\pm$2.0 for the BL Lacs and a highly dispersed 10 with a standard deviation of 12 for the FSRQs. However, without the four quasars exhibiting the largest values of maximum to mean fluxes (3C454.3, 1222+216, CTA102, and 3C273), the normalized maximum flux average for FSRQs drops to 5.0 $\pm$ 2.5. If the BL Lacs displayed such large amplitudes of γ-ray outbursts at the same rate as the FSRQs, we could expect, at least, 2 BL Lac objects with large outbursts. This implies that the process responsible for activity in the BL Lacs is more uniform, while the FSRQs appear to have different levels of activity.

3.2. Selection of Representative Epochs

To form a well-sampled, representative selection of data for a statistical study of spectral indices, we establish minimum requirements for epochs of data to be extracted for analysis. Because many objects have multiple epochs that can be classified as quiescent or active, and in order to avoid skewing the analysis towards any particular object, four epochs per object are selected for analysis for the majority of the sources, two within γ-ray quiescent periods and two within γ-ray active periods. Fewer than four epochs are used for ten sources because of either weak γ-ray emission and insufficient optical-UV data, or lack of simultaneity of observations across bands. An ideal epoch would include a sufficient number of observations to construct a complete SED and compute spectral indices for the γ-ray, X-ray, and UV-optical-NIR regions, although some epochs are accepted without X-ray measurements. Epochs are carefully selected to include a minimum separation of time between earliest and latest NIR through X-ray observations, never to exceed 24 hours, resulting in an average elapsed time of measurements for all selected epochs of 9.0 hours. Preference is given to epochs that include a wide range of NIR to UV wavebands and to epochs containing observations obtained from the greatest number of observatories to mitigate potential bias introduced by the use of data from a single observatory.

3.3. Light Curves and SEDs

Figure 4 presents the light curves of the quasar 1633+382 as an example of the data used in the analysis. (Light curves collected for all objects can be found in an expanded version of this paper at www.bu.edu/blazars/VLBAproject.html.) The light curves are presented in a series of sub-panels, with the highest frequency in the top panel and the lowest in the bottom panel. The energy range of the γ-ray flux is 0.1−200 GeV and of the X-ray flux, 0.3−10 keV. The observatory making the measurement is identified by the color and shape of the symbol. Table 2 presents the legend for the observatories. As explained in §3.2, up to four epochs per source were selected for analysis. These are indicated on the light curve plots by vertical dashed lines, with each epoch identified by a number and a color. Quiescent epochs are colored blue and green, active epochs are yellow and red. Horizontal dotted lines indicate upper limits of quiescent states and lower limits of active and flaring states.

Figure 5 presents SEDs for 0716+714 and 1633+382 as examples. (SEDs for all objects can be found in an expanded version of this paper at www.bu.edu/blazars/VLBAproject.html.) The SEDs display the flux data for each selected epoch, with the frequency adjusted to the rest frame of the host galaxy. Information about the selected epochs is given in Table 7, where column 1 is the object name, column 2 is the identifying epoch number (corresponding to the number displayed on the light curve plot), column 3 is the date of the earliest NIR − X-ray observation within the epoch, column 4 is the elapsed time in days between the earliest and the latest NIR − X-ray observations of the epoch, column 5 is the date of the center of the *Fermi* binned record, and column 6 is the bin size for that record. Columns 8-20 indicate the activity state of the object at different bands during the epoch: “Q” is quiescent, “A” is active, “F” is flaring, and “T” is transient. A dash indicates that although we had some data available for the band, there were fewer than 10 measurements and we did not compute $\langle F_\nu \rangle$. If there are multiple observations at a particular waveband, the activity state is determined based on the weighted mean of the observations.

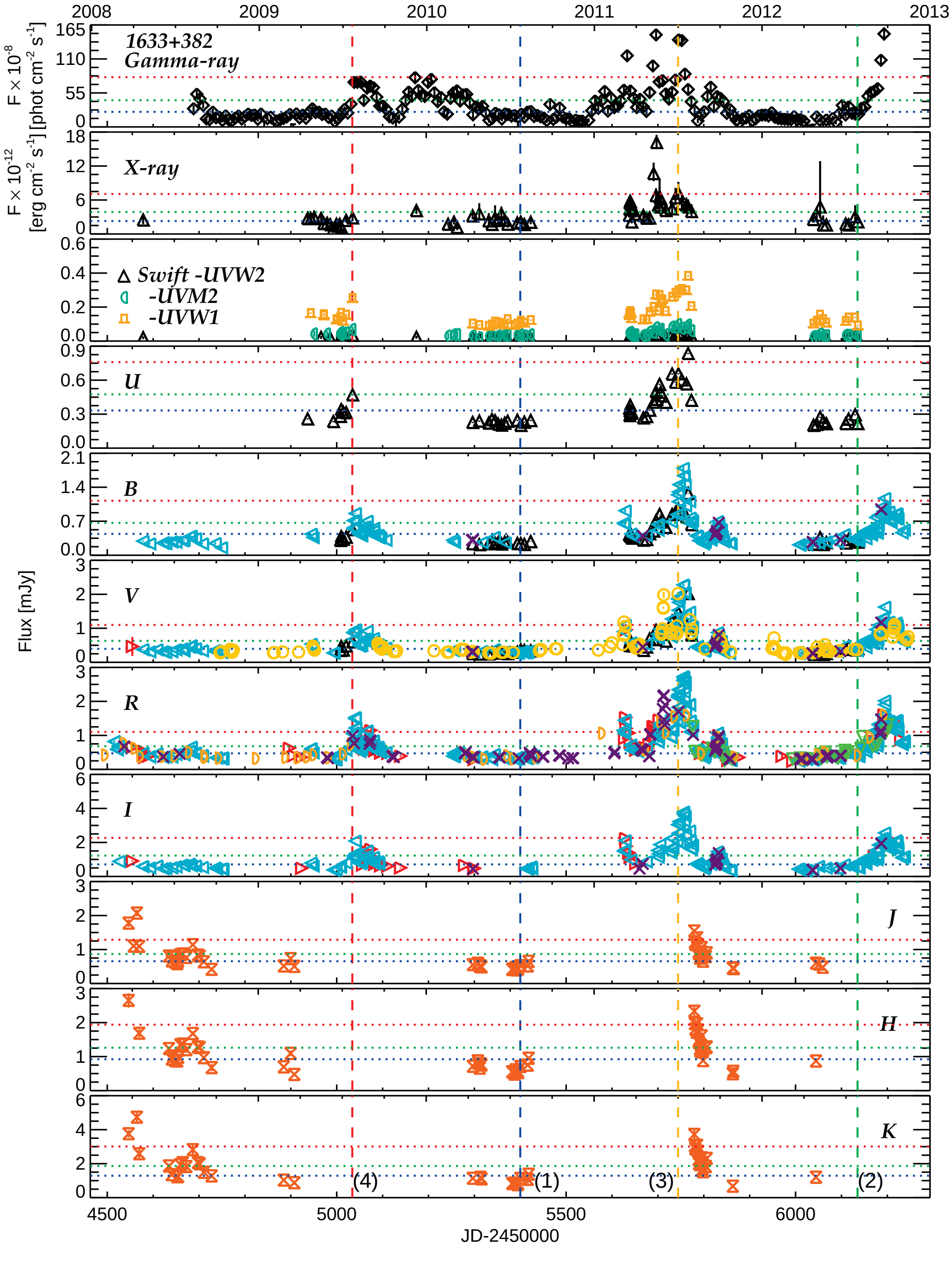

Fig. 4.—: Light curves at different wavebands from NIR to γ-ray frequencies, with 1633+382 presented as an example. Energy range of the γ-ray flux is 0.1−200 GeV and for X-ray flux, 0.3−10 keV. Symbols identify telescopes used in measurements (see Table 2). Horizontal dotted lines on the light curves indicate the upper limit for quiescent states (blue) and lower limits for active states (green) and flaring states (red). Vertical dashed lines indicate specific epochs of interest, each designated with an identifying number located in the lowest panel. [Light curves collected for all objects can be found in an expanded version of this paper at `www.bu.edu/blazars/VLBAproject.html`.]

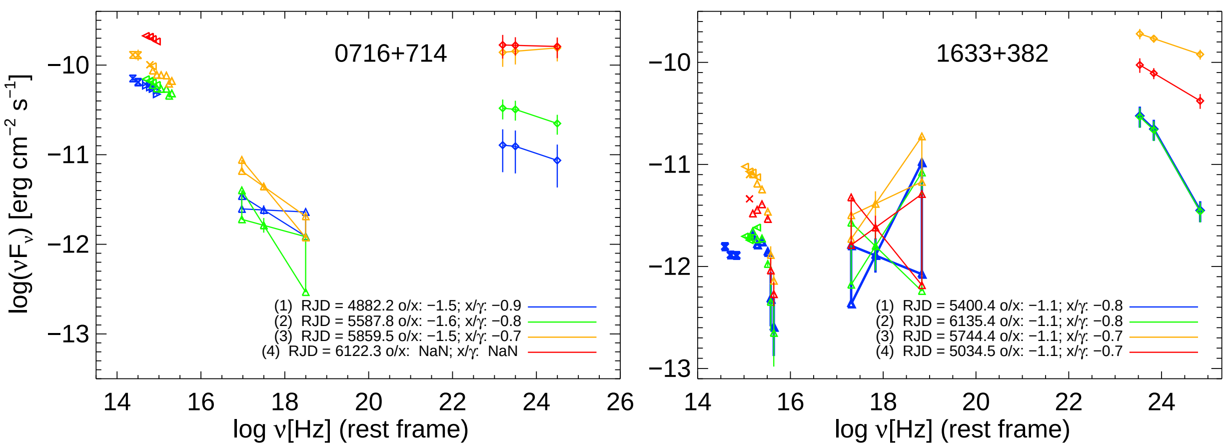

Fig. 5.—: SEDs for 0716+714 and 1633+382, shown as examples. Each epoch retains the identifying color and epoch number as displayed with vertical dashed lines on the light curves. The symbols (but not the color) refer to the observatory making the measurement (see Table 2). Frequency is adjusted to the object's rest frame. For convenience, α_{ox} and α_{xg} are shown if *Swift* X-ray data are available at the epoch. [SEDs for all objects can be found in an expanded version of this paper at `www.bu.edu/blazars/VLBAproject.html`.]

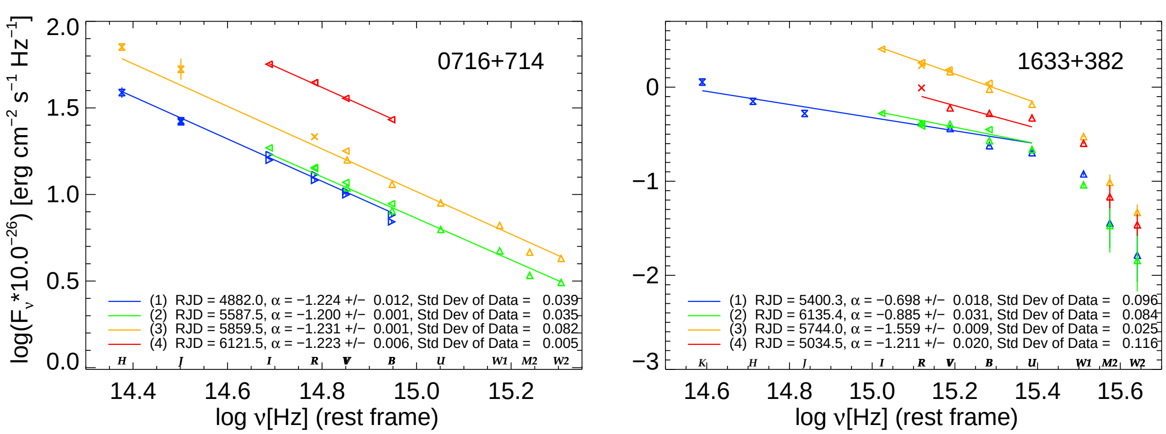

Fig. 6.—: Examples of optical spectral index computation. Each epoch retains the identifying color and epoch number as displayed with vertical dashed lines on the light curves. The symbols indicate the observatory (see Table 2). The frequency band of the observation is denoted immediately above the X-axis. Frequencies are adjusted for redshift.

Table 7

Epochs Selected For Study

Object Name	Epoch Number	Non-γ Observations Earliest Date Within Epoch	Elapsed Timespan	*Fermi* Obsvs. Mid-Bin Date	Bin Size	Activity State of Frequency Band *G*	*X*	*W2*	*M2*	*W1*	*U*	*B*	*V*	*R*	*I*	*J*	*H*	*K*
(1)	(2)	(3)	(4)	(5)	(6)	(7)	(8)	(9)	(10)	(11)	(12)	(13)	(14)	(15)	(16)	(17)	(18)	(19)
3C66A	1	5784.410	0.129	5781.048	7.0	Q	Q	Q	Q	Q	Q	Q	Q	Q	Q	Q	Q	Q
	2	6185.907	0.965	6187.048	7.0	Q						Q	Q	Q	Q			
	3	4744.658	0.763	4744.000	7.0	F	A	A	A	T	T	T	T	A	T			
	4	5390.561	0.977	5479.999	7.0	A						A	A	A	A	F	F	A
0235+164	1	5087.774	0.052	5087.996	7.0	Q	Q			Q		T	T	T		Q		Q
	2	5128.683	0.192	5130.009	7.0	Q						T	Q	Q	Q	Q		Q
	3	4729.762	0.393	4731.000	3.0	F	T	A	A	A	A	F	F	F		F		
	4	4758.502	0.970	4758.000	3.0	F	F	A	A	F	A	F	F	F		F	F	F
0336-019	1	4711.555	0.032	4714.500	5.5	Q							T	Q	Q			
	2	4917.231	0.109	4894.500	60.0	Q	-	-	-	-	-	Q	Q					
	3	5832.461	0.466	5831.644	7.0	A						T	A	T	T			
	4	5858.888	0.016	5859.644	7.0	F						A	F	A	A			
0420-014	1	5124.447	0.469	5123.009	7.0	Q						T	T	T	Q			
	2	5508.897	0.964	5512.509	32.5	Q	Q	Q	Q	Q	Q	Q	Q	Q				
	3	5217.245	0.082	5214.009	7.0	A						F	F	F	F			
	4	5899.334	0.015	5900.048	7.0	A						T	T	T	Q			
0528+134	1	5120.762	0.201	5122.000	7.0	Q						Q	Q	Q	T	Q		
	3	5825.600	0.407	5823.048	7.0	A						T	T	A	A			
0716+714	1	4882.182	0.371	4882.000	3.0	Q	Q					Q	Q	Q	Q	T	Q	
	2	5587.747	0.631	5588.000	3.0	Q	Q	Q	Q	Q	Q	Q	Q	Q	Q			
	3	5859.502	0.529	5860.000	3.0	A	T	T	T	T	T	T	T	T		F	A	
	4	6122.279	0.007	6183.000	3.0	A						F	F	A	A			
0735+178	1	5503.001	0.628	5501.009	7.0	Q	Q	Q	Q	-	Q	Q		Q		T	T	T
	2	6011.277	0.347	6012.048	7.0	Q							T	A	T			
	3	6070.398	0.244	6068.048	7.0	A	F	A	A	-	A	A	A	A				
0827+243	1	4767.528	0.501	4759.500	30.0	Q						Q	Q	Q				
	2	5503.630	0.365	5509.500	30.0	Q	A	Q	T	Q	Q		T	T		A	A	A
	3	6198.701	0.585	6201.041	7.0	A	A	A	A	A	A		A	F				
	4	6284.264	0.039	6285.041	7.0	F	F	A	A	A	A							
0829+046	1	5663.736	0.006	5655.510	30.0	Q						T	Q	Q	Q			
	2	6089.713	0.010	6090.541	30.0	Q	A	-			-		Q					
	3	5234.339	0.020	5235.044	7.0	A						F	A	A	A			
0836+710	1	5624.396	0.024	5627.028	14.0	Q						Q	T	T				
	2	6020.937	0.011	6023.506	7.0	Q	T	T	T	T	A	T	Q					
	3	5869.336	0.348	5870.047	7.0	F	T	T								Q	Q	Q
	4	5923.485	0.731	5926.047	7.0	F	F	T	T	T	T	T	Q	A				
OJ287	1	5296.542	0.837	5298.024	7.0	Q	Q	T	T	T	T	T	T	T	T	Q		Q
	2	5340.494	0.852	5340.024	7.0	Q	Q	Q	Q	Q	Q	Q	Q	Q	Q	Q		Q
	3	5129.847	0.567	5130.044	7.0	A	A	T	T	T	T	T	T	T	T	A		A
	4	6038.508	0.833	6040.041	7.0	A						A	A	A	A	A		A
0954+658	1	4766.685	0.918	4774.500	60.0	Q						Q	Q	Q		Q	Q	Q
	2	4781.697	0.006	4774.500	60.0	Q										Q	Q	Q
	3	5636.232	0.384	5634.028	7.0	A						A	F	A				
	4	5667.827	0.539	5669.028	7.0	F						A	A	A	A			
1055+018	1	5305.329	0.571	5306.542	30.0	Q	Q	-	-	-	-	T	Q	Q				
	2	6046.729	0.022	6047.028	7.0	Q						Q	Q	Q	-			
	3	5664.801	0.007	5662.010	7.0	A						A	A	A	-			
	4	5709.314	0.041	5711.010	7.0	A	A	-	-	-	-	F	A					
Mkn421	1	5306.337	0.010	5305.011	7.0	Q						Q	Q	Q				
	2	5729.351	0.017	5732.028	7.0	Q						Q	Q	Q				
	3	5319.355	0.024	5319.011	7.0	A	F	Q	Q	Q		Q	Q	Q				
	4	6123.294	0.017	6124.028	7.0	F						A	A	A				
1127-145	1	5193.997	0.214	5184.542	30.0	Q	T	T	T	T	-	Q	-					
	2	5926.442	0.353	5933.528	30.0	Q	Q	T		T	-	Q		A		A		
1156+295	1	5674.348	0.030	5676.028	7.0	Q						Q	Q	Q	Q			
	2	6038.659	0.785	6040.028	7.0	Q	A		-			T	A	A	T			
1219+285	1	5272.809	0.038	5270.011	7.0	Q	A	T	T	Q	Q	Q	Q					
	2	5988.436	0.151	5991.028	7.0	Q	Q	Q	Q	Q	Q	Q	Q	Q				
	3	4877.816	0.010	4875.655	7.0	A	T	A	A	A	A	A	A					
	4	4884.913	0.014	4882.655	7.0	A	F	A	A	A	A	A	A					
1222+216	1	5672.522	0.345	5675.992	7.0	Q	T	Q	Q	Q	Q	Q	Q	Q				
	2	6025.625	0.011	6026.048	7.0	Q	Q	Q	Q	Q	Q	Q	Q					
	3	5317.278	0.161	5319.009	7.0	F	Q				T			T				
	4	5369.145	0.223	5368.009	7.0	F	Q	A	A	A	A	A	A	A				

Table 7—*Continued*

Object Name (1)	Epoch Number (2)	Non-γ Observations Earliest Date Within Epoch (3)	Non-γ Observations Elapsed Timespan (4)	*Fermi* Obsvs. Mid-Bin Date (5)	*Fermi* Obsvs. Bin Size (6)	Activity State of Frequency Band *G* (7)	*X* (8)	*W*2 (9)	*M*2 (10)	*W*1 (11)	*U* (12)	*B* (13)	*V* (14)	*R* (15)	*I* (16)	*J* (17)	*H* (18)	*K* (19)
3C273	1	5295.660	0.896	5298.000	7.0	Q	T					Q	Q	Q	Q	Q		
	2	6045.359	0.491	6044.000	7.0	Q						F	T	T	Q	Q	Q	Q
	3	5207.592	0.264	5206.000	7.0	A	A					T	Q		Q	T		
	4	5272.526	0.459	5276.000	7.0	F	T					T	Q	Q	Q	A		
3C279	1	4966.580	0.940	4969.042	7.0	Q	Q	Q	Q	Q	Q	Q	Q	Q		Q		Q
	2	6011.463	0.398	6009.504	7.0	Q	T	Q	Q	Q	Q	T	Q	A				
	3	4898.744	0.798	4899.057	7.0	A	Q	Q	Q	Q	Q	Q	Q	T		T	A	T
	4	5665.659	0.600	5669.028	7.0	A	A	Q	Q	Q	Q	T	Q	A	T	A		T
1308+326	1	5302.082	0.386	5305.011	7.0	Q	Q	Q						Q				
1406-076	1	5294.737	0.007	5298.011	7.0	Q						T	Q	T		Q		
	2	5354.102	0.646	5354.011	7.0	Q	Q	A	Q	Q	T	Q	T	A				
1510-089	1	5714.774	0.754	5718.028	7.0	Q	Q	Q	Q	Q	Q	Q	Q	Q				
	2	6064.552	0.923	6068.028	7.0	Q	T	Q	T	T		Q	Q	T	Q	A		
	3	4918.487	0.476	4917.655	7.0	F	T	T	T	T	T	A	A	A	A	A		
	4	5747.276	0.093	5746.028	7.0	F	Q	Q	Q	Q	Q	Q	Q	T				
1611+343	1	5252.722	0.341	5256.011	7.0	Q	-	-	-	-	-	Q	T					
	2	5832.201	0.419	5830.028	7.0	Q						Q	T	T	Q			
1622-297	1	4745.490	0.005	4758.155	30.0	Q						Q	Q	T		Q		Q
	2	5350.951	0.728	5354.011	7.0	Q	T	T	A	T	A	T	T					
	3	5295.473	0.251	5298.011	7.0	A	A	T	Q	Q	A	T	Q	T		Q		Q
1633+382	1	5400.397	0.762	5402.000	7.0	Q	Q	Q	Q	Q	Q	Q	Q			Q	Q	Q
	2	6135.430	0.911	6137.000	7.0	Q	Q	Q	Q	Q	Q	Q	T	Q	Q			
	3	5744.449	0.387	5745.000	7.0	F	F	A	A	A	A	A	F	F	F			
	4	5034.519	0.212	5038.000	7.0	A	T	A	A	A	T	T	T	A				
3C345	1	5826.277	0.420	5820.528	18.5	Q						Q	Q	Q	Q			
	2	6036.932	0.587	6044.528	44.0	Q						Q	Q	Q	Q			
	3	5067.109	0.269	5067.042	7.0	A	Q	Q	Q	Q	Q	Q	T	A	T			
	4	5110.554	0.669	5109.042	7.0	A	Q	T	T	T	T	T	T	A	T			
1730-130	1	4980.711	0.156	4983.022	7.0	Q						Q	T	Q		Q		Q
	2	5376.704	0.005	5375.046	7.0	Q						A	Q	Q		T		T
	3	5433.603	0.734	5431.046	7.0	A						F	F	F				
	4	5494.502	0.002	5494.046	7.0	A						F	F	A		A		A
1749+096	1	6070.825	0.092	6072.155	30.0	Q								A		-		
	2	6135.326	0.125	6132.155	30.0	Q						Q	Q	A	T			
	3	5427.240	0.185	5428.655	7.0	A	T		Q			Q	Q	F	A			
	4	5502.790	0.803	5505.655	7.0	A	A	Q	Q	Q	Q	Q	Q	A				
BL Lacertae	1	5033.523	0.419	5036.655	7.0	Q	T	Q	Q	Q	Q	Q	Q	Q				
	2	5503.691	0.191	5505.655	7.0	Q	T	Q	Q	Q	Q	Q	Q	Q				
	3	5707.822	0.078	5704.048	7.0	F	T	A	A	A	A	A	A					
	4	6029.555	0.163	6030.506	7.0	A	T	A	A	A	A	A	A	A				
3C446	1	5341.606	0.073	5351.155	30.0	Q	-	-			-	A	T					
	2	5825.797	0.775	5817.155	30.0	Q						A	A		-			
CTA102	1	5126.709	0.047	5127.655	7.0	Q						Q	Q	Q	Q			
	2	5828.375	0.696	5827.655	7.0	Q	Q	Q	Q	Q	Q	Q	Q	Q	Q			
	3	6191.256	0.248	6194.030	7.0	F	A	T	T	T	T	T	T	T	A			
	4	6245.244	0.594	6243.030	7.0	F	F	A				A	A	A	F			
3C454.3	1	5729.702	0.840	5729.655	1.0	Q								Q				
	2	6180.576	0.836	6181.655	7.0	Q	Q	Q	Q	Q	Q	Q	Q	Q	Q			
	3	5167.194	0.340	5165.042	7.0	F	F	A	A	A	A	A	A	A		F		A
	4	5522.276	0.604	5522.042	7.0	F	A	A	A			A	A	F		F		F

Note.—Activity States: Q - Quiescent; T - Transitory; A - Active; F - Flaring; Blank - No data; "–" - Insufficient number of observations to calculate a mean flux value.

4. Computation of Spectral Indices

Optical Spectral Index

In the optical bands, we fit the blazar spectrum by a power law of the form

$$S_\nu \propto \nu^{\alpha_o}, \tag{2}$$

where S_ν is the radiative flux density at frequency ν and α_o is the spectral index at optical wavelengths. We note that the optical spectrum that we fit with a single power law can include multiple components (emission lines, BBB, synchrotron radiation), the implication of which will be discussed in Section 6. To compute α_o, we perform a weighted linear least-square fit using the IDL routine `LINFIT`, combining all data available in the UV−NIR range unless there is an obvious break in the power law in either the NIR or UV bands. We retrieve the slope and its error and report these as α_o and σ_{α_o}, respectively. Examples of the fit are shown in Figure 6 for two objects.

Because we assume the model to be linear, testing the goodness of the fit to the model in the usual sense is not very meaningful in this case. The weighted χ^2 statistic would be quite large given the small value of many of our uncertainties. To provide some measure of the "goodness of fit," we compute the standard deviation of the data, σ, using

$$\sigma^2 = \frac{1}{N-2}\Sigma(y_i - \bar{y})^2, \tag{3}$$

where N is the number of data points, $y_i = \log\ S_\nu$, and $\bar{y}$ is the computed best-fit value (Bevington & Robinson 2003), with two parameters determined from the fit.

X-Ray and Gamma-Ray Photon Indices

Both the X-ray and γ-ray spectral indices are computed from the power-law photon index, Γ, as $\alpha = \Gamma + 1$. For γ-ray observations, Γ_γ is derived differently depending upon whether the epoch corresponds to a quiescent or an active state. For quiescent epochs, we extract from the 2FGL catalog (Nolan et al. 2012) the photon index and its uncertainty. (Note: the spectra of some sources were also fit with a log parabolic model, in which case the uncertainty in α_γ is not given in the 2FGL catalog and, therefore, is not listed in the table.) For active states, we calculate Γ_γ values from the photon and spacecraft data (see Section 2.2).

Broadband Spectral Slopes

Two additional spectral indices are of interest to our study: the slope between optical and X-ray frequencies, α_{ox}, and the slope between X-ray and γ-ray energies, α_{xg}. We use the weighted mean of the fluxes in V band for the optical emission. If no V-band observations are available, preference is given to measurements in the *R, J, B, UVM2*, or *UVW1* bands, in that order. We use X-ray and γ-ray emission at 1 keV and 0.5 GeV, respectively, to represent the high energies.

The computed spectral indices for all objects are summarized in Table 8: column 1 is the object name, column 2 is the identifying epoch number (corresponding to the number displayed on the light curve plot), column 3 is the date of the earliest observation (among X-ray - NIR measurements) within the epoch, columns 4−9 are α_γ, α_X, and α_o, and their respective 1-σ uncertainties, column 10 provides the number of UV−optical−NIR observations included in the computation of α_o, and column 11 lists the standard deviation of the data relative to the best-fit line (the measurement of the "goodness of fit" of the spectral slope for α_o). Columns 12−15 are α_{ox} and α_{xg} and their respective 1-σ uncertainties. Column 16 indicates the frequency band used in the computation of α_{ox} if no V-band observation is available.

Table 8
Computed Spectral Indices

Object Name (1)	Epoch Number (2)	Earliest Non-γ Obsv.in Epoch (3)	α_γ (4)	σ_{α_γ} (5)	α_X (6)	σ_{α_x} (7)	α_o (8)	σ_{α_o} (9)	# UV-opt-NIR pts (10)	Std. Dev. of Data (11)	α_{ox} (12)	$\sigma_{\alpha_{ox}}$ (13)	α_{xg} (14)	$\sigma_{\alpha_{xg}}$ (15)	α_o Band (16)
3C66A	1	5784.410	-0.912		-1.559	0.253	-1.292	0.002	14	0.007	-1.503	0.026	-0.780	0.012	
	2	6185.907	-0.912				-1.044	0.019	6	0.022					
	3	4744.658	-0.893	0.085	-1.971	0.129	-0.872	0.001	10	0.057	-1.443	0.010	-0.757	0.005	
	4	5390.561	-0.746	0.098			-0.811	0.004	8	0.059					
0235+164	1	5087.774	-1.124		-1.120	0.338	-1.586	0.013	6	0.017	-1.130	0.047	-0.769	0.022	
	2	5128.683	-1.124				-1.791	0.009	10	0.122					
	3	4729.762	-0.990	0.078	-1.237	0.460	-1.726	0.003	8	0.084	-1.409	0.051	-0.674	0.024	
	4	4758.502	-1.056	0.087	-1.679	0.174	-1.627	0.002	10	0.081	-1.115	0.018	-0.812	0.008	
0336-019	1	4711.555	-1.475	0.072			-0.260	0.051	5	0.001					
	2	4917.231	-1.475	0.072	-0.924	0.677	-0.366	0.030	4	0.022	-1.154	0.063	-0.860	0.029	
	3	5832.461	-1.104	0.217			-1.009	0.023	9	0.001					
	4	5858.888	-1.225	0.130			-0.948	0.023	4	0.007					
0420-014	1	5124.447	-1.298	0.028			-1.330	0.025	11	0.003					
	2	5508.897	-1.298	0.028	-0.984	0.367	-0.807	0.031	7	0.049	-1.038	0.050	-0.811	0.023	
	3	5217.245	-0.870	0.132			-1.146	0.073	6	0.007					
	4	5899.334	-1.369	0.196			-1.616	0.065	4	0.030					
0528+134	1	5120.762	-1.545				-0.719	0.030	9	0.025					
	3	5825.600	-1.545				-0.446	0.029	7	0.039					
0716+714	1	4882.182	-1.077		-1.159	0.136	-1.224	0.012	11	0.039	-1.517	0.020	-0.873	0.009	
	2	5587.747	-1.077		-1.436	0.309	-1.200	0.001	11	0.035	-1.591	0.031	-0.771	0.014	
	3	5859.502	-0.962	0.086	-1.450	0.119	-1.231	0.001	11	0.082	-1.489	0.013	-0.737	0.006	
	4	6122.279	-1.013	0.135			-1.223	0.006	5	0.005					
0735+178	1	5503.001	-1.047	0.035	-1.294	0.481	-1.519	0.007	9	0.035	-1.502	0.065	-0.754	0.031	R
	2	6011.277	-1.047	0.035			-1.477	0.017	5	0.011					
	3	6070.398	-1.374	0.248	-1.223	0.379	-0.975	0.006	7	0.033	-1.246	0.037	-0.808	0.017	
0827+243	1	4767.528	-1.674	0.070			-0.548	0.070	6	0.010					
	2	5503.630	-1.674	0.070	-0.697	0.108	-0.482	0.013	7	0.038	-1.001	0.018	-0.937	0.008	
	3	6198.701	-1.268	0.229	-0.577	0.095	-0.890	0.011	3	0.000	-1.080	0.014	-0.801	0.007	
	4	6284.264	-1.304	0.097	-0.703	0.178	-0.974	0.031	4	0.083	-1.046	0.039	-0.770	0.015	UVM2
0829+046	1	5663.736	-1.181				-1.729	0.011	4	0.036					
	2	6089.713	-1.181		-0.430	0.454	-1.501	0.015	3	0.038	-1.444	0.081	-0.804	0.037	
	3	5234.339	-1.217	0.273			-1.596	0.011	5	0.006					
0836+710	1	5624.396	-1.948	0.073			-0.629	0.039	4	0.001					
	2	6020.937	-1.948	0.073	-0.468	0.102	-0.282	0.022	3	0.006	-0.797	0.021	-1.016	0.010	
	3	5869.336	-1.607	0.081	-0.438	0.095	-0.904	0.114	3	0.003	-0.766	0.014	-0.790	0.007	J
	4	5923.485	-1.609	0.172	-0.451	0.085	-0.453	0.023	5	0.067	-0.714	0.013	-0.928	0.006	
OJ287	1	5296.542	-1.232	0.043	-1.259	0.163	-1.338	0.002	19	0.075	-1.426	0.017	-0.863	0.008	
	2	5340.494	-1.232	0.043	-1.279	0.173	-1.528	0.003	11	0.032	-1.347	0.020	-0.848	0.009	
	3	5129.847	-1.392	0.176	-0.885	0.069	-1.582	0.002	12	0.038	-1.339	0.010	-0.821	0.005	
	4	6038.508	-1.229	0.164			-1.425	0.002	20	0.016					
0954+658	1	4766.685	-1.415	0.067			-1.329	0.022	7	0.017					
	2	4781.697	-1.415	0.067			-1.242	0.062	3	0.022					J
	3	5636.232	-1.076	0.218			-1.805	0.020	16	0.116					
	4	5667.827	-1.292	0.253			-1.769	0.071	17	0.037					
1055+018	1	5305.329	-1.217	0.039	-0.998	0.408	-1.509	0.019	8	0.074	-1.164	0.050	-0.860	0.023	
	2	6046.729	-1.217	0.039			-1.438	0.015	5	0.001					
	3	5664.801	-1.243	0.190			-1.418	0.008	4	0.007					
	4	5709.314	-1.434	0.252	-0.718	0.179	-1.581	0.009	6	0.023	-1.248	0.023	-0.799	0.011	
Mkn421	1	5306.337	-0.771	0.012			-0.521	0.046	5	0.001					
	2	5729.351	-0.771	0.012			-0.575	0.055	4	0.000					
	3	5319.355	-0.770	0.089	-1.061	0.012	-0.419	0.063	4	0.000	-0.717	0.004	-1.166	0.002	
	4	6123.294	-0.747	0.046			-0.587	0.024	4	0.000					
1127-145	1	5193.997	-1.697	0.051	-0.388	0.111	-0.646	0.012	4	0.049	-1.120	0.021	-0.953	0.010	
	2	5926.442	-1.697	0.051	-0.665	0.559	-0.331	0.018	4	0.031	-1.001	0.048	-0.957	0.025	J
1156+295	1	5674.348	-1.295	0.027			-1.112	0.043	5	0.018					
	2	6038.659	-1.295	0.027	-0.584	0.528	-1.216	0.024	17	0.008	-1.345	0.102	-0.775	0.048	
1219+285	1	5272.809	-1.019	0.034	-1.704	0.252	-0.911	0.003	7	0.019	-1.348	0.028	-0.908	0.013	
	2	5988.436	-1.019	0.034	-1.622	0.440	-1.264	0.004	7	0.009	-1.554	0.043	-0.837	0.020	
	3	4877.816	-0.965	0.156	-1.686	0.441	-1.022	0.002	6	0.055	-1.550	0.040	-0.786	0.019	
	4	4884.913	-1.470	0.205	-1.776	0.170	-0.973	0.002	6	0.049	-1.402	0.016	-0.848	0.008	
1222+216	1	5672.522	-1.231		-0.592	0.254	-0.146	0.004	6	0.013	-1.359	0.035	-0.787	0.016	
	2	6025.625	-1.231		-0.814	0.484	-0.040	0.005	4	0.017	-1.364	0.086	-0.748	0.040	
	3	5317.278	-0.982	0.035	-0.828	0.237	-0.305	0.009	3		-1.377	0.036	-0.521	0.017	R
	4	5369.145	-1.078	0.024	-0.669	0.258	-0.363	0.004	6	0.094	-1.473	0.036	-0.482	0.017	

TABLE 8—*Continued*

Object Name (1)	Epoch Number (2)	Earliest Non-γ Obsv.in Epoch (3)	α_γ (4)	σ_{α_γ} (5)	α_X (6)	σ_{α_x} (7)	α_o (8)	σ_{α_o} (9)	# UV-opt-NIR pts (10)	Std. Dev. of Data (11)	α_{ox} (12)	$\sigma_{\alpha_{ox}}$ (13)	α_{xg} (14)	$\sigma_{\alpha_{xg}}$ (15)	α_o Band (16)
3C273	1	5295.660	-1.616		-0.658	0.043	-0.458	0.004	8	0.024	-1.236	0.006	-1.035	0.003	
	2	6045.359	-1.616				-0.564	0.070	4	0.041					
	3	5207.592	-1.431	0.074	-0.664	0.026	-0.422	0.003	4	0.019	-1.165	0.004	-0.915	0.002	
	4	5272.526	-1.492	0.088	-0.693	0.044	-0.494	0.003	9	0.010	-1.223	0.005	-0.898	0.003	
3C279	1	4966.580	-1.340		-0.797	0.131	-1.696	0.007	12	0.040	-0.924	0.017	-0.862	0.008	
	2	6011.463	-1.340		-0.550	0.178	-1.578	0.008	12	0.102	-1.115	0.028	-0.895	0.013	
	3	4898.744	-1.419	0.083	-0.875	0.215	-1.770	0.006	13	0.036	-1.096	0.028	-0.742	0.013	
	4	5665.659	-1.908	0.152	-0.665	0.092	-1.747	0.005	16	0.054	-1.081	0.014	-0.763	0.006	
1308+326	1	5302.082	-1.222		-0.250	0.718	-1.517	0.206	3	0.002	-1.159	0.171	-0.757	0.081	R
1406-076	1	5294.737	-1.429	0.064			-0.851	0.042	4	0.045					
	2	5354.102	-1.429	0.064	-0.742	1.843	-1.401	0.104	4	0.012	-1.134	0.180	-0.779	0.084	
1510-089	1	5714.774	-1.388		-0.489	0.587	-0.628	0.008	8	0.022	-1.213	0.083	-0.727	0.039	
	2	6064.552	-1.388		-0.835	0.422	-0.721	0.006	14	0.041	-1.150	0.073	-0.770	0.034	
	3	4918.487	-1.244	0.025	-0.394	0.139	-1.104	0.004	17	0.161	-1.309	0.021	-0.550	0.010	
	4	5747.276	-1.268	0.046	-0.585	0.146	-0.710	0.007	9	0.026	-1.201	0.021	-0.573	0.010	
1611+343	1	5252.722	-1.307	0.171	-0.443	0.578	-0.461	0.059	4	0.003	-1.208	0.092	-0.920	0.042	
	2	5832.201	-1.307	0.171			-0.422	0.014	11	0.023					
1622-297	1	4745.490	-1.339	0.067			-0.647	0.043	4	0.010					
	2	5350.951	-1.339	0.067	-0.397	0.557	-0.466	0.026	5	0.026	-1.283	0.056	-0.791	0.026	
	3	5295.473	-1.423	0.230	-0.301	0.399	-0.490	0.025	6	0.082	-1.114	0.042	-0.782	0.020	
1633+382	1	5400.397	-1.410		-0.637	0.546	-0.698	0.018	6	0.096	-1.073	0.064	-0.760	0.029	
	2	6135.430	-1.410		-0.859	0.581	-0.885	0.031	8	0.084	-1.055	0.090	-0.777	0.042	
	3	5744.449	-1.155	0.058	-0.562	0.223	-1.559	0.009	9	0.025	-1.109	0.046	-0.708	0.021	
	4	5034.519	-1.270	0.084	-1.118	0.446	-1.211	0.020	4	0.116	-1.052	0.044	-0.721	0.020	
3C345	1	5826.277	-1.489	0.056			-1.438	0.030	7	0.033					
	2	6036.932	-1.489	0.056			-1.493	0.062	7	0.005					
	3	5067.109	-1.073	0.174	-0.859	0.135	-1.515	0.017	8	0.022	-1.090	0.022	-0.782	0.010	
	4	5110.554	-1.319	0.334	-0.578	0.246	-1.291	0.024	5	0.027	-1.193	0.028	-0.770	0.013	
1730-130	1	4980.711	-1.488				-0.937	0.019	6	0.058					
	2	5376.704	-1.488				-1.520	0.027	5	0.073					
	3	5433.603	-1.440	0.103			-2.385	0.134	4	0.006					
	4	5494.502	-1.132	0.087			-1.061	0.074	3	0.001					
1749+096	1	6070.825	-1.243				-1.536	0.012	7	0.030					R
	2	6135.326	-1.243				-1.717	0.028	8	0.018					
	3	5427.240	-1.267	0.198	-0.422	0.179	-1.767	0.025	9	0.060	-1.404	0.026	-0.766	0.012	
	4	5502.790	-1.394	0.148	-0.579	0.141	-2.066	0.014	7	0.007	-1.155	0.024	-0.853	0.011	
BL Lacertae	1	5033.523	-1.261		-0.957	0.182	-1.745	0.005	9	0.012	-1.350	0.019	-0.854	0.009	
	2	5503.691	-1.261		-0.854	0.112	-1.694	0.006	8	0.021	-1.323	0.015	-0.884	0.007	
	3	5707.822	-1.240	0.074	-0.790	0.157	-1.640	0.002	7	0.022	-1.486	0.019	-0.749	0.009	
	4	6029.555	-1.070	0.083	-0.913	0.083	-1.619	0.002	7	0.052	-1.506	0.010	-0.772	0.005	
3C446	1	5341.606	-1.436	0.053	0.217	0.825	-0.650	0.087	3	0.006	-1.030	0.123	-0.857	0.057	
	2	5825.797	-1.436	0.053			-0.679	0.025	4	0.006					
CTA102	1	5126.709	-1.538				-0.254	0.011	7	0.011					
	2	5828.375	-1.538		-0.377	0.158	-0.413	0.005	16	0.008	-1.150	0.024	-0.820	0.011	
	3	6191.256	-1.006	0.034	-0.616	0.084	-1.108	0.005	18	0.034	-1.098	0.014	-0.619	0.007	
	4	6245.244	-1.396	0.080	-0.514	0.120	-1.409	0.008	6	0.055	-1.177	0.019	-0.760	0.009	
3C454.3	1	5729.702	-1.379		-0.566	0.140	-0.889	0.007	9	0.115	-1.151	0.022	-0.752	0.010	
	2	6180.576	-1.379		-0.984	0.357	-1.053	0.010	9	0.092	-1.163	0.051	-0.842	0.024	
	3	5167.194	-1.344	0.023	-0.584	0.039	-1.352	0.001	9	0.031	-0.972	0.006	-0.749	0.003	
	4	5522.276	-1.259	0.010	-0.602	0.040	-1.548	0.003	6	0.041	-1.057	0.007	-0.630	0.003	

5. Trends and Correlations of Spectral Indices

5.1. Distributions of Spectral Indices

Figure 7 presents distributions of the spectral indices α_o, α_X, and α_γ, and the spectral index between these regions, α_{ox} and α_{xg}. We compute a mean of each spectral index from our selected epochs for each class in each state. The results are summarized in Table 9. The standard deviation is a good indicator of the spread of the indices. We consider a deviation within $\pm$ 0.35 ($\sim$ 20% of the approximate spread of all indices) to be a sufficiently narrow spread to indicate a "preferred" value for the index.

For α_o, only BL Lacs in a quiescent state maintain a preferred value. For α_X, both the quiescent and the active FSRQs exhibit small deviations, with a preferred value of ~ -0.6, as expected if the X-ray emission is produced via inverse Compton scattering by relatively low energy electrons that also emit synchrotron emission at millimeter-submillimeter (mm-submm) wavelengths. Active BL Lacs have a significant scatter in α_X, with some values as steep as -2. This can be explained by a synchrotron origin of the enhanced X-ray emission in some BL Lacs. Quiescent BL Lacs exhibit a preferred value of -1.2, which suggests that the quiescent X-ray emission is a mixture of IC and synchrotron emission.

Both quiescent and active states of both classes exhibit a preferred value of the γ-ray spectral index. The BL Lacs show little difference in α_γ between quiescent and active states. Ackermann et al. (2011) found a similar mean value for BL Lacs with a range from -0.90 to -1.17, depending upon the SED classification (LSP, ISP, HSP). The FSRQs show a modest flattening of α_γ during active states. Ackermann et al. (2011) computed a mean value for FSRQs of -1.42 ± 0.17 for a much larger sample, which falls between the average values of α_γ during quiescent and active states.

Both quiescent and active states of both classes exhibit preferred values of the spectral index between the optical and X-ray and between the X-ray and γ-ray regimes. The preferred values of α_{ox} change little within each class between states, while they are different for the two classes. The preferred values of α_{xg} are similar for the BL Lacs and FSRQs within the 1σ uncertainty, independent of the state.

5.2. Change of Spectral Indices between States

To study the change of spectral indices between states, we compute the difference between the spectral indices of quiescent and active states for each object (between the means of α in the cases of two quiescent and two active states identified). Histograms of these differences are presented in Figure 8. The FSRQs tend to have a separation between quiescent and active states in both optical and γ-ray spectra, while the differences between states for the BL Lacs tend to be equally distributed. Of the active FSRQs, 80% have a flatter average γ-ray spectrum, with a weighted mean difference from the average quiescent spectrum of 0.16. (Some caution must be applied in this case, however, because Γ_γ is allowed to vary for the active states, while we use a fixed value taken from the 2FGL catalog for each object in quiescent states.) Abdo et al. (2010b) found a weak "harder when brighter" effect for all FSRQs and BL Lacs except the HSP subclass, as had been previously suggested by Ghisellini et al. (2009) for both classes when comparing some measurements from *Fermi* and EGRET. For our sample of blazars, a significant "harder when brighter" effect is seen in the γ-ray spectral index for FSRQs, but the BL Lacs show no propensity towards a flatter or steeper spectrum, nor is there any obvious trend with SED class.

Of the quiescent FSRQs, 73% tend to have flatter optical spectra than during active states, while there is no statistical difference for α_o of BL Lacs between the two states. The difference in behavior of α_o for FSRQs implies an important contribution of the emission from the accretion disk (BBB) to the optical quiescent radiation, while accretion disk emission in BL Lacs seems to be too weak to play a significant role in the SED. In support of this latter point, the average value of α_o of ~ -1.4 in active and quiescent BL Lacs indicates dominance of synchrotron emission during all states. This conforms with the prediction of Giommi et al. (2012a), who simulated SEDs of blazars with a varying mix of Doppler-boosted radiation from the jet with emission from the ac-

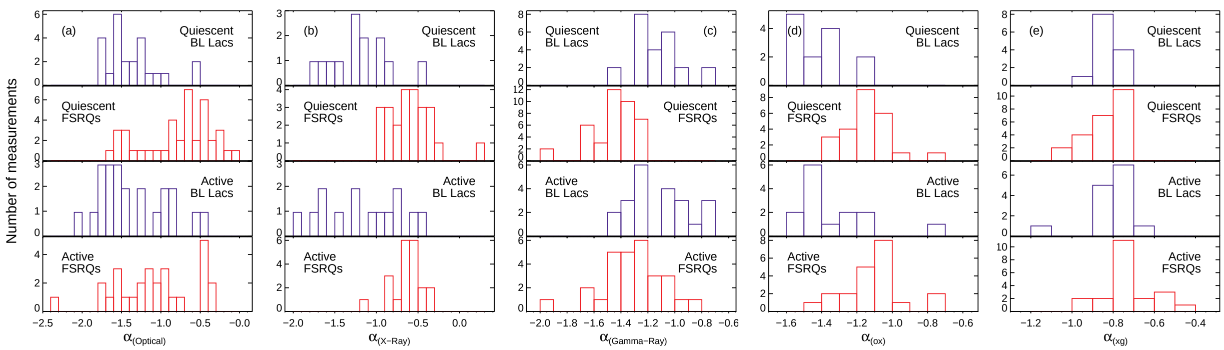

Fig. 7.—: Distributions of spectral indices for quiescent and active states: (a) optical, (b) X-ray, (c) γ-ray, (d) optical − X-ray, and (e) X-ray − γ-ray. FSRQs are plotted in red; BL Lac objects in blue.

TABLE 9
MEAN VALUES OF SPECTRAL INDICES

Spectral Index (1)	Quiescent BL Lac (2)	Quiescent FSRQ (3)	Active BL Lac (4)	Active FSRQ (5)
α_o				
Average Value	−1.4	−0.8	−1.4	−1.1
Standard Deviation	0.3	0.4	0.4	0.5
α_X				
Average Value	−1.2	−0.60	−1.2	−0.63
Standard Deviation	0.3	0.27	0.5	0.18
α_γ				
Average Value	−1.12	−1.46	−1.13	−1.31
Standard Deviation	0.17	0.17	0.23	0.22
α_{ox}				
Average Value	−1.40	−1.13	−1.32	−1.11
Standard Deviation	0.14	0.13	0.22	0.17
α_{xg}				
Average Value	−0.83	−0.84	−0.81	−0.73
Standard Deviation	0.05	0.09	0.11	0.12

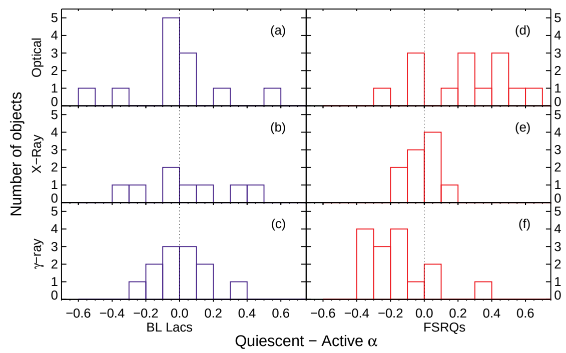

Fig. 8.—: Distribution of difference of spectral indices between quiescent and active states for BL Lac objects (*left*, blue) and FSRQs (*right*, red), panels (a) and (d) for α_o, (b) and (e) for α_X, and (c) and (f) for α_γ.

cretion disk, broad-line region, and light from the host galaxy, and found strong dominance of the jet emission in BL Lacs.

The differences of the X-ray spectral indices of FSRQs between states are equally distributed with a negligible mean of 0.001, as is evident in Figure 8e. This suggests that the same mechanism(s) is (are) employed for the X-ray production in FSRQs, independent of the state. In BL Lacs, the IC X-ray spectrum generally has a slope flatter than −1, whereas the slope is generally steeper for X-ray synchrotron radiation (e.g. Bregman et al. 1990).

The very broad scatter of α_X (quiescent) - α_X (active) for BL Lacs indicates: (i) an increase in the contribution of synchrotron emission during active states for some BL Lacs (e.g., 3C66A, the largest positive difference); (ii) flattening of α_X at active states for another group of BL Lacs (e.g., OJ287, the largest negative difference) that corresponds to an increase of the contribution of IC emission; and (iii) no change of α_X for the rest of BL Lacs. Although we cannot correlate the behavior with the SED subclasses of BL Lacs due to an insufficient amount of statistical data, the BL Lacs of the LSP type tend to have flatter X-ray spectra during active states.

5.3. Relationships Between Spectral Indices

We examine relationships between the spectral indices at the different wavebands. Figures 9, 10, 11, & 12 show dependences between α_γ and α_o, α_γ and α_X, α_X and α_o, and between α_{ox} and α_{xg}, respectively, for all blazars in the sample. The complete set of all plots in color and labeled with object and epoch numbers can be found in an expanded version of this paper at `www.bu.edu/blazars/VLBAproject.html`. We have computed Spearman's rank correlation coefficients between different spectral indices for the entire sample, as well as for different classes and states. We have used the IDL routine `R_Correlate` to test the significance of the correlation coefficients. The results are presented in Table 10, with the number of data points in the computation and the rank correlation coefficient and its significance given for each relationship.

The α_γ*–*α_o *Plane*: Figure 9 reveals a striking difference between the quiescent BL Lacs and FSRQs: a BL Lac object with a flatter α_o has a flatter α_γ, while for the quasars a modest anticorrelation between the indices is observed. The correlation analysis (Table 10) confirms a highly significant positive correlation between α_γ and α_o of the BL Lacs independent of the state, and suggests a weak anti-correlation between α_γ and α_o of the quiescent FSRQs at ∼88.5% confidence level. The latter effect disappears in active FSRQs. We associate flattening of α_o in FSRQs with increasing importance of the BBB contribution to the optical emission when the synchrotron flux decreases. If we assume that a pure synchrotron optical spectral index correlates with α_γ, as in the case of the BL Lacs, then the anti-correlated behavior between α_γ and α_o for the quiescent FSRQs implies that quasars with a stronger BBB have a softer optical synchrotron spectrum. This is supported by the case of 3C273, in which the BBB dominates the optical-UV SED, while the synchrotron spectral index, as measured for the linearly polarized emission, is very steep, −1.7 to −2.7 (Smith et al. 1993). However, the steep optical synchrotron index found for the quasar 3C454.3 during the prominent γ-ray outbursts, $\alpha_o^{syn} \sim -1.7$, is significantly steeper than $\alpha_\gamma \sim -1.3$ (Jorstad et al. 2013); this implies that relativistic electrons that emit IR synchrotron radiation rather than optical emission are responsible for γ-ray production.

There are outliers in Figure 9 that are important to mention. Quasar 1730−130 at epoch 3 and BL Lac object 1749+096 at epoch 4 (both active states) have extremely steep optical spectra (−2.4 and −2.1, respectively), and a follow-up study of additional active epochs of these objects could be enlightening. Active epoch 4 of 3C279 has a steep γ-ray spectrum (−1.9), while all epochs of 1222+216 are located in the flat optical−flat γ-ray region of both the active and quiescent FSRQs.

The $\alpha_\gamma - \alpha_X$ *Plane*: Figure 10 shows a distinct separation in the $\alpha_\gamma - \alpha_X$ plane for the two classes of blazars, with only a slight overlap. This is obviously driven by the separation of X-ray spectral index values between classes as discussed in §5.1. Combining classes yields strong anti-correlations for both active (Fig. 10c) and quiescent (Fig. 10d) states. Quiescent BL Lacs show a strong anti-correlation between α_γ and α_X, that becomes very weak for active BL Lacs (Table 10). In general, for a blazar in our sample, steeper α_X pairs with flatter α_γ. Within IC mechanisms for γ-ray production, this suggests that for sources with a synchrotron origin of X-rays (fully or partly), lower-energy relativistic electrons participate in γ-ray production (those that generate IR-optical synchrotron emission), while for sources with X-rays via IC mechanisms, higher-energy relativistic electrons should be involved in 0.1−200 GeV γ-ray production (those that produce optical-UV synchrotron emission).

There are outliers in the $\alpha_\gamma - \alpha_X$ plane that include three BL Lacs that are well known TeV sources: 1219+285, 3C66A, and Mkn421. Among the FSRQs, the quasars 3C279 and 0836+710 are distinguished by the steepness of their γ-ray spectra. Additionally, the first quiescent epoch of 3C446 is isolated in the region of flat X-ray spectra ($\alpha_X = 0.22$), although the uncertainty in the index is high.

The $\alpha_X - \alpha_o$ *Plane*: Figure 11a shows a strong anti-correlation between α_X and α_o for BL Lacs, independent of activity state, with a high confidence level (see Table 10). According to the discussion in §5.1, values of α_o of the BL Lacs should represent pure synchrotron spectra. The observed anti-correlation and steepness of α_X, up to −2.0, imply that in BL Lacs with the hardest optical spectra, the X-ray emission is produced via the synchrotron mechanism. These are the TeV sources Mkn421, 1219+285 and 3C66A mentioned above. As the optical spectrum softens, the contribution from IC mechanisms to the X-ray emission increases. In general, there is no overlap between the BL Lacs and FSRQs in Figures 11(c,d), since the FSRQs have flatter values of α_o, indicating the presence of the BBB, and uniformly flat values of α_X that point to IC mechanisms for X-ray production. However, some active BL Lacs with the flattest α_X form a continuation of the sequence of active FSRQs into the steepest α_o values. These are among the brightest BL Lacs at radio wavelengths, 1749+096, BL Lacertae, 1055+018 and OJ287. Three quiescent quasars with the steepest α_o values form a continuation of the quiescent BL Lac sequence into the flattest α_X values (3C 279, 1308+326, and 1406−076), which most likely have weaker BBB emission with respect to the jet emission than for the other FSRQs.

The $\alpha_{ox} - \alpha_{xg}$ *Plane*: An anti-correlation is expected in this plane if 1) the X-ray flux varies with much higher amplitude than do the optical and γ-ray fluxes, or 2) the optical and γ-ray fluxes vary in unison while the X-ray flux is relatively stable in many of the sources. Neither case commonly occurs (see Table 4). According to Table 10 there is a statistically significant anti-correlation between α_{ox} and α_{xg} for active BL Lacs. However, the anti-correlation is driven by the spectral indices of Mkn 421, which is the only HSP source in our sample. The rest of the BL Lacs show very small scatter in the values of α_{xg}, with slightly flatter values during active states. Table 9 shows that the average values of α_{xg} of FSRQs are similar to those of BL Lacs. The stability of α_{xg} follows from the high ratio of γ-ray to X-ray frequencies, the logarithm of which is in the denominator of the X-ray – γ-ray spectral index calculation. In this context, the line of active quasars in Figures 12b,c with α_{xg} flatter than −0.7 is especially interesting, since these are the quasars with the strongest amplitude of γ-ray activity: 1222+216, 1510-089, CTA102, 3C454.3, and 0836+710 (see Figure 3). The line shows a clear anti-correlation between α_{ox} and α_{xg}, which corresponds to case 2 above and implies that the γ-ray and optical fluxes have significantly larger amplitudes of variation than that of the X-ray emission. This is not expected

Table 10

Spearman's Rank Correlation (ρ)

	α_γ and α_o			α_γ and α_x			α_x and α_o			α_{xg} and α_{ox}		
	n	ρ	Signif.	n	ρ	Signif.	n	ρ	Signif.	n	ρ	Signif.
(1)	(2)	(3)	(4)	(5)	(6)	(7)	(8)	(9)	(10)	(11)	(12)	(13)
BL Lac Quiescent	24	0.572	0.004	13	-0.776	0.002	13	-0.676	0.011	13	-0.269	0.374
BL Lac Active	22	0.473	0.026	14	-0.442	0.114	14	-0.631	0.016	14	-0.732	0.003
All BL Lacs	46	0.504	3.6E-04	27	-0.556	0.003	27	-0.648	2.6E-04	27	-0.395	0.041
FSRQ Quiescent	40	-0.253	0.115	24	-0.055	0.799	24	0.105	0.625	24	-0.437	0.033
FSRQ Active	28	0.029	0.883	21	-0.239	0.297	21	0.113	0.626	21	-0.458	0.037
All FSRQ	68	-0.258	0.034	45	-0.134	0.379	45	0.078	0.609	45	-0.289	0.054
All Quiescent	64	-0.445	2.3E-04	37	-0.594	1.1E-04	37	0.405	0.013	37	-0.238	0.156
All Active	50	0.086	0.552	35	-0.428	0.010	35	0.060	0.731	35	-0.216	0.212
All	114	-0.256	0.006	72	-0.499	8.3E-06	72	0.233	0.049	72	-0.180	0.129

Note.—n: number of indices included in the computation; ρ: rank correlation coefficient; *Signif*: the two-sided significance level.

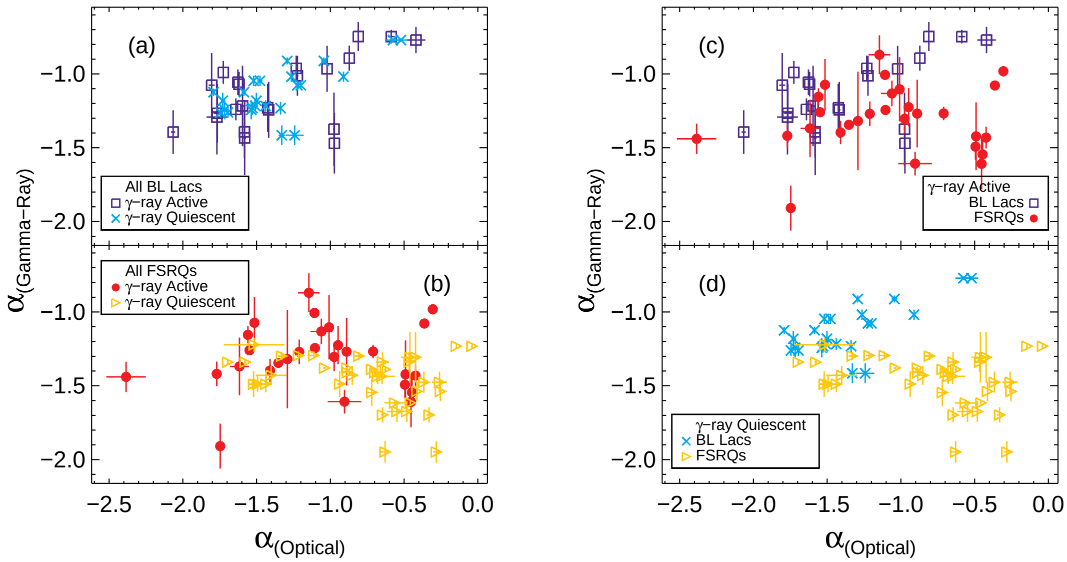

Fig. 9.—: Spectral indices α_γ vs. α_o at selected epochs (Section 3.2) for all blazars in the sample: FSRQs are red-filled circles in γ-ray active states, yellow triangles if quiescent, while BL Lacs are dark blue squares if γ-ray active, light blue if quiescent. Panels are: (a) all BL Lacs, (b) all FSRQs, (c) active BL Lacs and FSRQs, and (d) quiescent BL Lacs and FSRQs. [A combined plot with each data point labeled with object and epoch numbers is printed at the end of this manuscript. A complete set of individual plots, with each data point labeled with object and epoch numbers can be found in an expanded version of this paper at `www.bu.edu/blazars/VLBAproject.html`.]

if the SSC mechanism is responsible for both the X-ray and γ-ray emission, since in this case the value of α_{xg} should remain stable across activity states. The significant difference in the amplitude of X-ray and γ-ray activity might be caused by different seed photons being scattered by the relativistic electrons: synchrotron from the jet for X-rays (SSC) and external for γ-rays (EC). Alternatively, the X-ray variations could be smoothed out by longer timescales of energy losses of the relatively low-energy electrons participating in IC X-ray production. There is a clear separation between the BL Lacs and FSRQs with respect to values of α_{ox}, especially for the quiescent blazars (Figure 12d): the FSRQs possess flatter α_{ox} values than those of BL Lacs. This supports the conclusion that different X-ray emission mechanisms operate in the BL Lacs and FSRQs, as pointed out in the analysis of the $\alpha_X - \alpha_o$ plane.

6. Discussion: Implications for Emission Models

The analysis of spectral indices in each waveband and the relationship between these indices allow us to describe a "typical" BL Lac object or FSRQ and contrast the results by activity state within each class. Table 11 summarizes statistically significant results from this exercise.

Our findings suggest that the optical emission of a "typical" BL Lac object is strongly dominated by synchrotron radiation at any state, independent of SED classification. This implies that any emission from the accretion disk is weak in BL Lacs, consistent with the polarimetry of BL Lacs showing no evidence for the wavelength-dependent polarization expected when the essentially unpolarized BBB contributes substantially to the optical-UV emission (e.g., Smith & Sitko 1991; Smith 1996).

The X-ray emission from BL Lacs is a mixture of synchrotron and IC radiation. The statistically

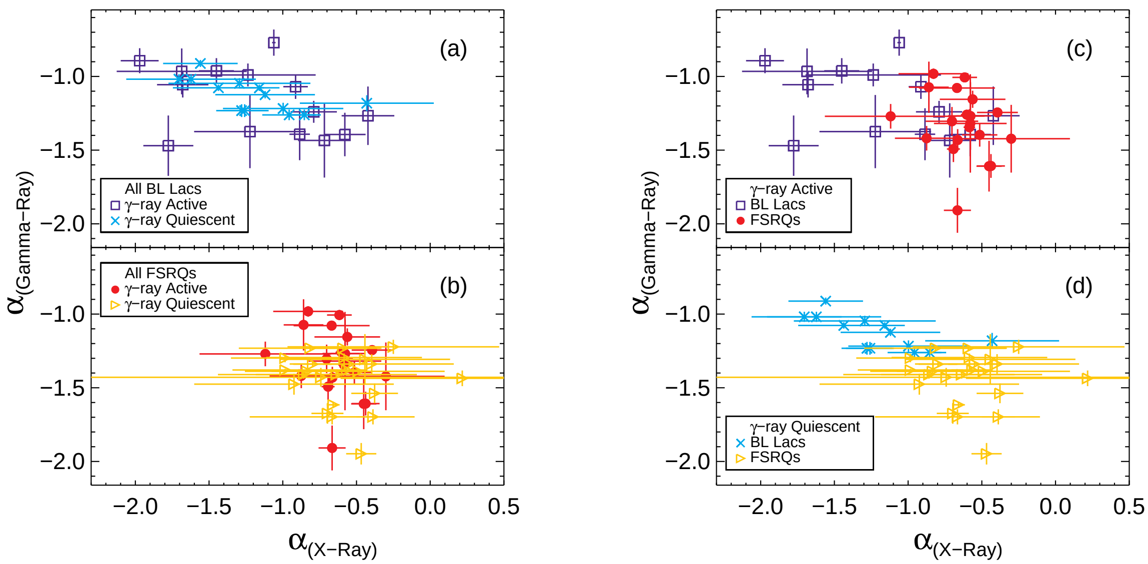

Fig. 10.—: Spectral indices α_γ vs. α_X. Designations are the same as in Fig. 9.

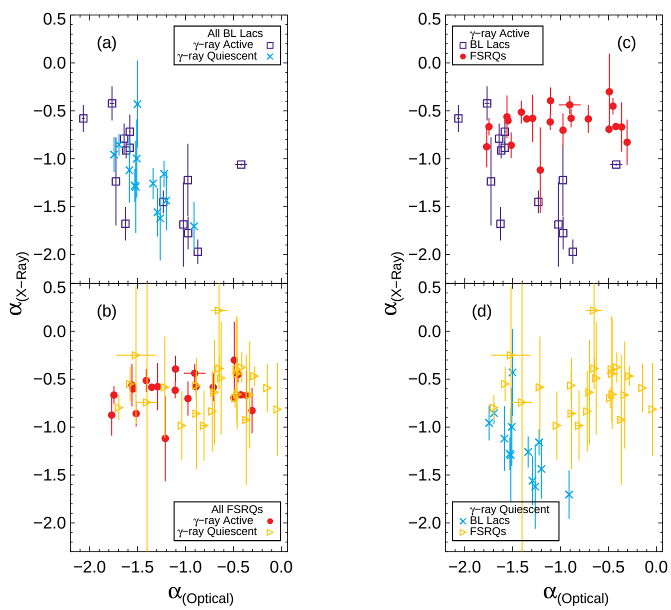

Fig. 11.—: Spectral indices α_X vs α_o. Designations are the same as in Fig. 9.

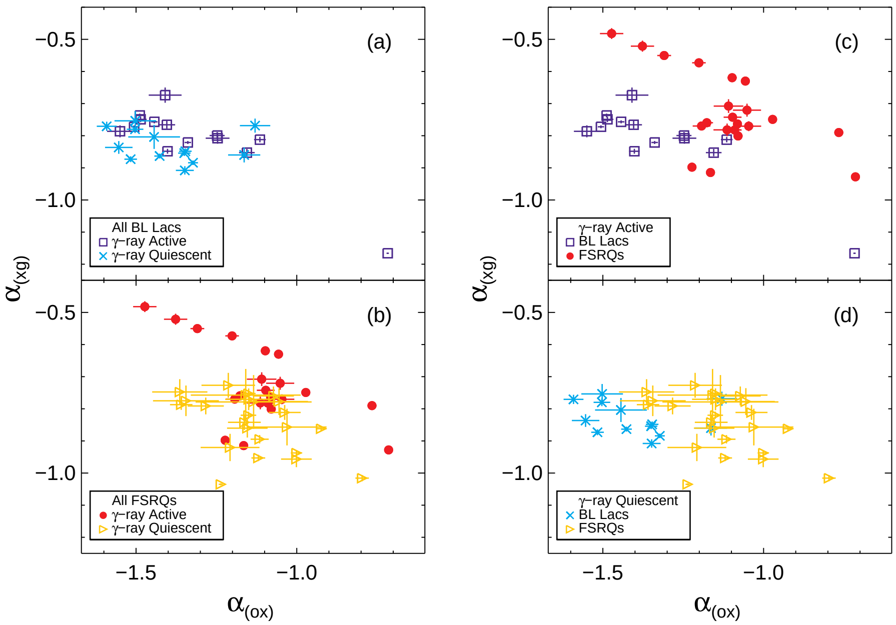

Fig. 12.—: Spectral indices α_{xg} vs α_{ox}. Designations are the same as in Fig. 9.

Table 11

"Typical" Quiescent or Active Object

	"Typical" BL Lac		"Typical" FSRQ	
	Quiescent	Active	Quiescent	Active
(1)	(2)	(3)	(4)	(5)
Mean value:				
α_o	-1.4 ± 0.3	high dispersion	high dispersion	high dispersion
α_X	-1.2 ± 0.3	high dispersion	-0.60 ± 0.27	-0.63 ± 0.18
α_γ	-1.12 ± 0.17	-1.13 ± 0.23	-1.46 ± 0.17	-1.31 ± 0.22
α_{ox}	-1.40 ± 0.14	-1.32 ± 0.22	-1.13 ± 0.13	-1.11 ± 0.17
α_{xg}	-0.83 ± 0.05	-0.81 ± 0.11	-0.84 ± 0.09	-0.73 ± 0.12
Correlation probability:				
α_γ and α_o	99.6%	97.4%	88.5% (anti)	ns
α_γ and α_X	99.8% (anti)	88.6% (anti)	ns	ns
α_X and α_o	98.9% (anti)	98.4% (anti)	ns	ns
α_{ox} and α_{xg}	ns	99.7% (anti)	96.7% (anti)	96.3% (anti)
Percentage time in state:	$55 \pm 20\%$	$9 \pm 4\%$	$65 \pm 15\%$	$10 \pm 8\%$
Longest uninterrupted period:				
Average number of days	216	43	217	30
Normalized amplitude of γ-ray variations:		5.2 ± 2.0		10 ± 12

Note.—*ns*: not significant.

significant correlation between α_o and α_X implies that the contribution of IC emission to the observed X-rays increases as the optical spectrum softens, especially for active BL Lacs. The optical and γ-ray spectral indices are correlated at $> 97\%$ confidence level. No difference in values of α_γ between quiescent and active states is observed, which implies that the same mechanism is responsible for quiescent and flaring γ-ray emission. The modest amplitude of γ-ray activity, with small scatter across the BL Lac sample, favors the SSC mechanism for γ-ray production, while slightly flatter values of α_γ relative to α_o imply that relativistic electrons radiating at both optical and IR wavelengths are involved.

A "typical" FSRQ has a flatter optical spectrum in quiescent than in active states, which can be attributed to the importance of the contribution of the BBB to the optical-UV continuum (e.g., Smith et al. 1988; Giommi et al. 2012b). The wide dispersion of optical spectral indices is then due to diversity in the relative strength of the BBB among FSRQs rather than to variations in the slope of their synchrotron spectra. We anticipate that once the BBB component is subtracted, the residual synchrotron spectral index will show a smaller scatter in α_o, as in BL Lacs, and also as is the case for α_γ for both the BL Lacs and FSRQs. A modest anti-correlation between α_γ and α_o for the quiescent FSRQs implies a possible connection between the properties of the BBB and jet if the anti-correlation is driven by the contribution of the BBB to the optical emission. The latter is probable, since the anti-correlation disappears during active states. In this scenario, a quasar with a stronger BBB has softer optical synchrotron and γ-ray spectra in quiescent states. The γ-ray spectrum of an FSRQ flattens during active states, which implies more efficient acceleration of relativistic electrons if the γ-rays originate via IC mechanisms. This should cause flattening of the optical synchrotron spectra during active states as well. However, to test such an assumption and a possible connection between BBB and jet properties, pure synchrotron optical spectra of FSRQs should be extracted from the observations by subtracting the BBB spectrum from the continuum.

We find a uniform preferred value of $\alpha_X \sim -0.6$, among the FSRQs that is the same as the average spectral index of blazars measured at wavelengths of 0.8 to 4 mm (Giommi et al. 2012b). This supports the hypothesis that IC scattering from relativistic electrons emitting synchrotron radiation at mm-submm wavelengths is responsible for X-ray production in a typical FSRQ, independent of the activity state. Whether the X-rays are from the SSC or EC mechanism, or a combination of the two, might depend on the blazar and its activity state. The large dispersion in the amplitude of γ-ray activity, and the anti-correlated behavior between α_{xg} and α_{ox} for the FSRQs displaying the highest amplitude of γ-ray outbursts, require different mechanisms of γ-ray production during different activity states. There is most likely a mixture of SSC and EC emission, with a dominance of external IC during the highest γ-ray states, as has been modeled for some blazars (e.g., Bonnoli et al. 2011; Wehrle et al. 2012).

7. Summary

We have assembled—and de-reddened at NIR, optical and UV wavelengths—observational measurements obtained from 2008 through 2012 of 33 blazars by ten ground- and space-based observatories. We have computed a mean flux value for each frequency band for each source and used these values to determine whether the object was in a quiescent or active state in each band. The state of the object in the γ-ray band was the basis for defining quiescent and active periods. The frequency and length of quiescent and active periods, and the maximum flux achieved during active periods, were compared between the BL Lacs and FSRQs. Up to four epochs per source were selected for further analysis of spectral indices at γ-ray, X-ray, and, optical wavelengths. All IR through X-ray observations selected for an epoch were obtained within a 24-hour period, with an average span of 9.0 hours. We find significant diversity in the properties of the BL Lacs and FSRQs in each spectral regime analyzed:

1. The FSRQs exhibit the highest amplitude of γ-ray activity, while the duration of an average active period in the source frame is similar for the FSRQs and BL Lacs. On the other hand, the fraction of time when a quasar is dormant exceeds that of a BL Lac object by $\sim$10%, with less scatter.

2. Comparison of the behavior of α_o between activity states suggests weak accretion disk emission in the BL Lacs, while the contribution of the BBB to the optical emission of the FSRQs dominates quiescent states.

3. The lack of significant variations in γ-ray spectral indices of the BL Lacs between activity states, the relatively low ratio of γ-ray to synchrotron luminosity, and the good correlation between α_γ and α_o, implies that the same inverse Compton mechanism — most likely SSC — is responsible for the γ-ray production at different activity states.

4. The anti-correlation between α_{xg} and α_{ox} for the FSRQs during the most extreme activity at γ-ray energies suggests that the SSC mechanism is insufficient to explain the enhanced γ-ray flux in these objects. Hence, the EC mechanism for γ-ray (but not necessarily X-ray) production is favored by the data.

5. The analysis of X-ray spectral indices indicates that the X-ray emission of the BL Lacs is a mixture of synchrotron and inverse Compton radiation. IC scattering dominates during active states of the LSP BL Lacs, while IC scattering by < 1 GeV electrons can explain the entire X-ray emission of the FSRQs at any state.

The relationships among the various spectral indices therefore imply strong connections between the emission at pairs of wavebands: mm-submm and X-ray for FSRQs and LSP BL Lacs, optical and X-ray for ISP and HSP BL Lacs, and IR-optical and γ-ray for FSRQs and LSP BL Lacs. These connections should be apparent in timing studies of multi-waveband light curves of blazars. We are in the process of compiling such light curves over a sufficiently long time span (~ 5 years) to test whether the predictions of such correlations are fulfilled.

We thank the anonymous referee for providing valuable comments and suggestions that improved several sections of the paper. The data acquisition and analysis for this study was supported by National Science Foundation grant AST-0907893, NASA Fermi Guest Investigator grants NNX08AV65G, NNX09AT99G, NNX10AO59G, NNX10AV15G, NNX11AO37G, NNX11AQ03G, NNX12AO90G, and NASA Swift Guest Investigator grants NNX09AR11G, NNX10AL13G, NNX10AF88G, NNX12AF09G, and NNX12AE90G. The effort at Steward Observatory was funded in part by NASA through Fermi Guest Investigator grants NNX08AW56G, NNX09AU10G, and NNX12AO93G. The St. Petersburg State University team acknowledges support from RFBR grants 12-02-00452 and 12-02-31193. The research at the IAA-CSIC is supported by the Spanish Ministry of Economy and Competitiveness and the Regional Government of Andalucía (Spain) through grants AYA2010-14844 and P09-FQM-4784, respectively. The *Swift* effort at PSU is supported by NASA contract NAS5-00136. The PRISM camera at Lowell Observatory was developed by K. Janes et al. at BU and Lowell Observatory, with funding from the NSF, BU, and Lowell Observatory. The Liverpool Telescope is operated on the island of La Palma by Liverpool John Moores University in the Spanish Observatorio del Roque de los Muchachos of the Instituto de Astrofisica de Canarias, with funding from the UK Science and Technology Facilities Council. The Calar Alto Observatory is jointly operated by the Max-Planck-Institut für Astronomie and the Instituto de Astrofísica de Andalucía-CSIC. This study is partly based on data taken and assembled by the WEBT collaboration and stored in the WEBT archive at the Osservatorio Astronomico di Torino - INAF (http://www.oato.inaf.it/blazars/webt/).

Facilities: Perkins, Liverpool:2m, CAO:2.2m, Bok, SO:Kuiper, CTIO:1.3m, Swift, FERMI (LAT)

REFERENCES

Abdo, A. A., Ackermann, M., Ajello, M., et al. 2009, ApJ, 700, 597

—. 2010a, ApJ, 722, 520

—. 2010b, ApJ, 710, 1271

Abdo, A. A., Ackermann, M., Agudo, I., et al. 2010c, ApJ, 716, 30

Ackermann, M., Ajello, M., Allafort, A., et al. 2011, ApJ, 743, 171

Ackermann, M., Ajello, M., Ballet, J., et al. 2012, ApJ, 751, 159

Agudo, I., Molina, S. N., Gómez, J. L., et al. 2012, International Journal of Modern Physics Conference Series, 8, 299

Atwood, W. B., Abdo, A. A., Ackermann, M., et al. 2009, ApJ, 697, 1071

Bevington, P. R., & Robinson, D. K. 2003, Data reduction and error analysis for the physical sciences

Bonnoli, G., Ghisellini, G., Foschini, L., Tavecchio, F., & Ghirlanda, G. 2011, MNRAS, 410, 368

Böttcher, M., Reimer, A., Sweeney, K., & Prakash, A. 2013, ApJ, 768, 54

Bregman, J. N., Glassgold, A. E., Huggins, P. J., et al. 1986, ApJ, 301, 708

—. 1990, ApJ, 352, 574

Burrows, D. N., Hill, J. E., Nousek, J. A., et al. 2005, Space Sci. Rev., 120, 165

Chatterjee, R., Bailyn, C. D., Bonning, E. W., et al. 2012, ApJ, 749, 191

Danforth, C. W., Nalewajko, K., France, K., & Keeney, B. A. 2013, ApJ, 764, 57

D'Elia, V., Padovani, P., & Landt, H. 2003, MNRAS, 339, 1081

Dickey, J. M., & Lockman, F. J. 1990, ARA&A, 28, 215

Do, T., Ghez, A. M., Morris, M. R., et al. 2009, ApJ, 691, 1021

Fitzpatrick, E. L. 1999, PASP, 111, 63

Gehrels, N., Chincarini, G., Giommi, P., et al. 2004, ApJ, 611, 1005

Ghisellini, G., Maraschi, L., & Tavecchio, F. 2009, MNRAS, 396, L105

Giommi, P., Padovani, P., Polenta, G., et al. 2012a, MNRAS, 420, 2899

Giommi, P., Polenta, G., Lähteenmäki, A., et al. 2012b, A&A, 541, A160

Hagen-Thorn, V. A., Larionov, V. M., Jorstad, S. G., et al. 2008, ApJ, 672, 40

Hayashida, M., Madejski, G. M., Nalewajko, K., et al. 2012, ApJ, 754, 114

Jorstad, S. G., Marscher, A. P., Stevens, J. A., et al. 2007, AJ, 134, 799

Jorstad, S. G., Marscher, A. P., Larionov, V. M., et al. 2010, ApJ, 715, 362

Jorstad, S. G., Marscher, A. P., Joshi, M., et al. 2012, ArXiv e-prints

Jorstad, S. G., Marscher, A. P., Smith, P. S., et al. 2013, ApJ, 773, 147

Larionov, V. M., Jorstad, S. G., Marscher, A. P., et al. 2008, A&A, 492, 389

Madejski, G., Takahashi, T., Tashiro, M., et al. 1996, ApJ, 459, 156

Mannucci, F., Basile, F., Poggianti, B. M., et al. 2001, MNRAS, 326, 745

Marscher, A. P. 2012, ArXiv:1201.5402

Marscher, A. P., Jorstad, S. G., D'Arcangelo, F. D., et al. 2008, Nature, 452, 966

Marscher, A. P., Jorstad, S. G., Larionov, V. M., et al. 2010, ApJ, 710, L126

Mead, A. R. G., Ballard, K. R., Brand, P. W. J. L., et al. 1990, A&AS, 83, 183

Nalewajko, K. 2013, MNRAS, 430, 1324

Nilsson, K., Pasanen, M., Takalo, L. O., et al. 2007, A&A, 475, 199

Nolan, P. L., Abdo, A. A., Ackermann, M., et al. 2012, ApJS, 199, 31

Palma, N. I., Böttcher, M., de la Calle, I., et al. 2011, ApJ, 735, 60

Poole, T. S., Breeveld, A. A., Page, M. J., et al. 2008, MNRAS, 383, 627

Raiteri, C. M., Villata, M., Ibrahimov, M. A., et al. 2005, A&A, 438, 39

Raiteri, C. M., Villata, M., Larionov, V. M., et al. 2007, A&A, 473, 819

—. 2008a, A&A, 491, 755

—. 2008b, A&A, 480, 339

Raiteri, C. M., Villata, M., Smith, P. S., et al. 2012, A&A, 545, A48

Roming, P., Kennedy, T., Mason, K., et al. 2005, Space Science Reviews, 120, 95

Schlafly, E. F., & Finkbeiner, D. P. 2011, ApJ, 737, 103

Smith, P. S. 1996, in Astronomical Society of the Pacific Conference Series, Vol. 110, Blazar Continuum Variability, ed. H. R. Miller, J. R. Webb, & J. C. Noble, 135

Smith, P. S., Balonek, T. J., Heckert, P. A., & Elston, R. 1986, ApJ, 305, 484

Smith, P. S., Elston, R., Berriman, G., Allen, R. G., & Balonek, T. J. 1988, ApJ, 326, L39

Smith, P. S., Montiel, E., Rightley, S., et al. 2009, ArXiv e-prints

Smith, P. S., Schmidt, G. D., & Allen, R. G. 1993, ApJ, 409, 604

Smith, P. S., & Sitko, M. L. 1991, ApJ, 383, 580

Tagliaferri, G., Foschini, L., Ghisellini, G., et al. 2008, ApJ, 679, 1029

Tavecchio, F., Ghisellini, G., Bonnoli, G., & Ghirlanda, G. 2010, MNRAS, 405, L94

Wehrle, A. E., Marscher, A. P., Jorstad, S. G., et al. 2012, ApJ, 758, 72

This 2-column preprint was prepared with the AAS LaTeX macros v5.2.

Supplemental Material

The following plots combine panels a − d of Figures 9 − 12, with each data point labeled with object and epoch numbers, included in this version for your convenience.

An expanded version of this paper with a complete set of light curves, SEDs, and labeled spectral index relationship plots for all sources can be found at `www.bu.edu/blazars/VLBAproject.html`.

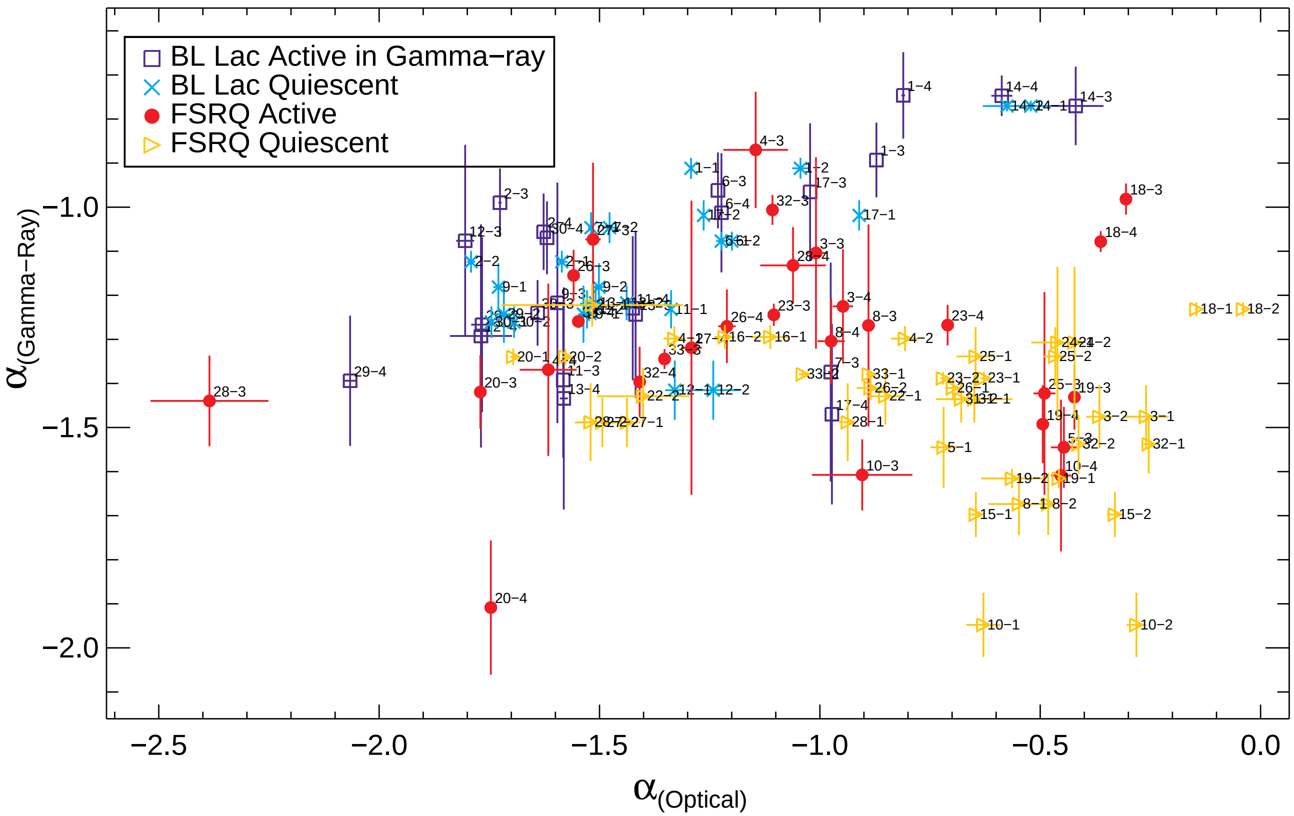

Fig. 13.—: Spectral indices α_γ vs. α_o at selected epochs (Section 3.2) for all blazars in the sample: FSRQs are red circles in γ-ray active states, yellow if quiescent, while BL Lacs are dark blue if γ-ray active, light blue if quiescent. Each data point is labeled with object and epoch numbers (see Table 1) and epoch numbers (see Table 7).

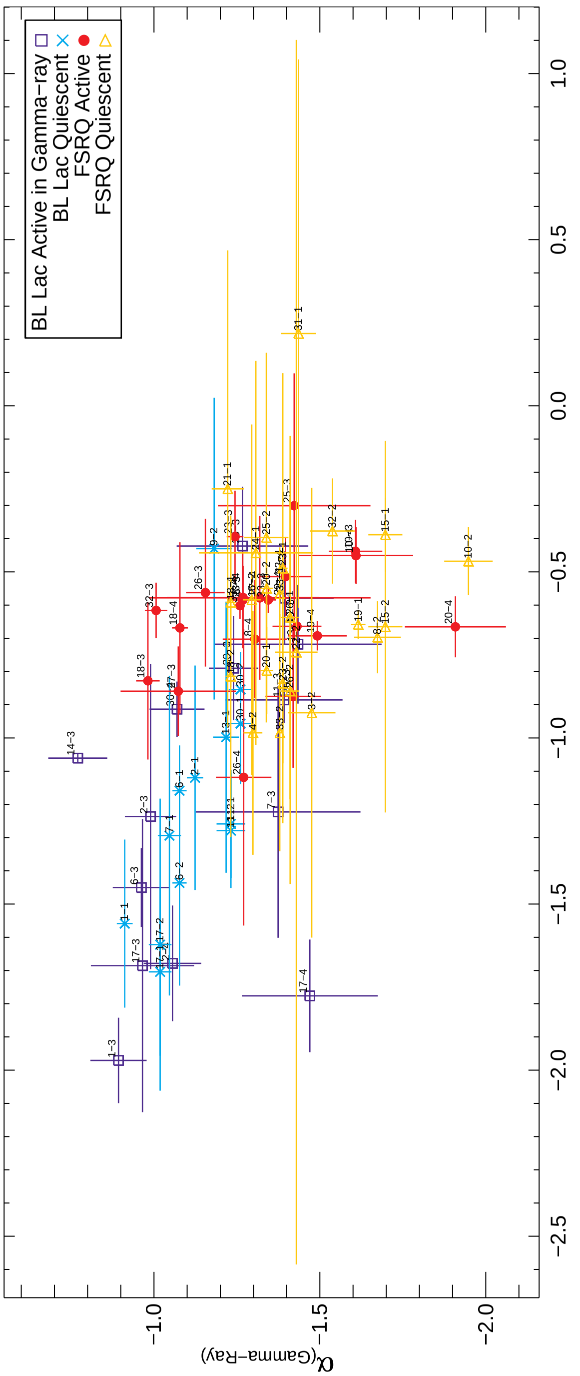

Fig. 14.—: Spectral indices α_γ vs. α_X. Designations are the same as in Fig. 13.

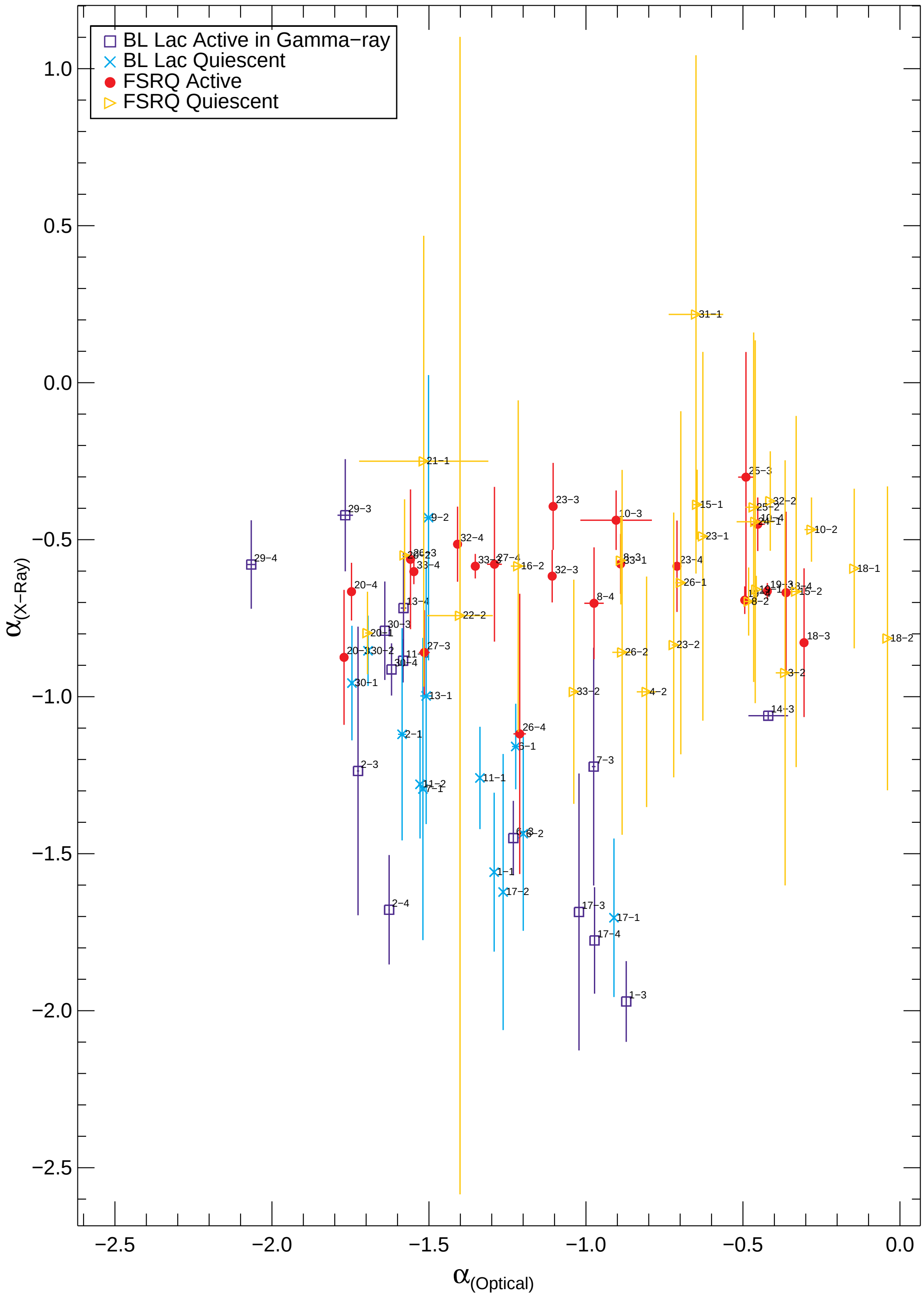

Fig. 15.—: Spectral indices α_X vs α_o. Designations are the same as in Fig. 13.

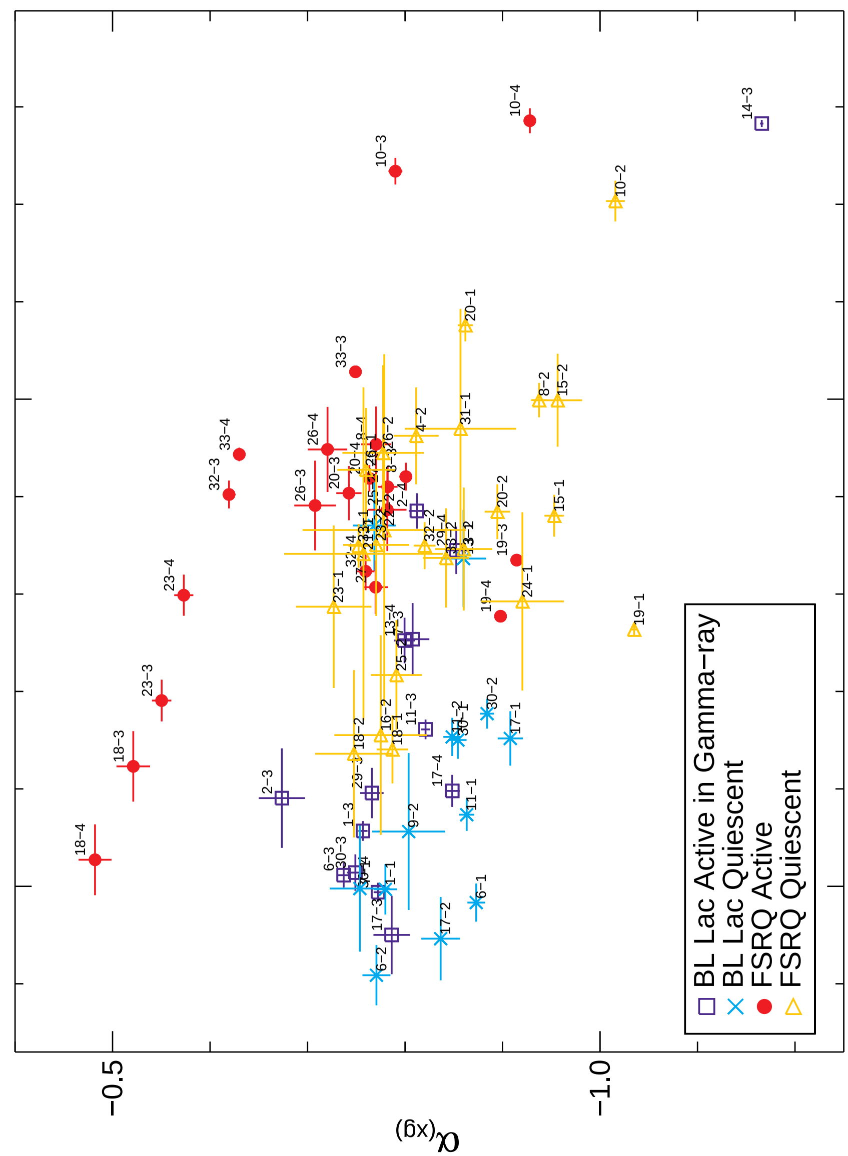

Fig. 16.—: Spectral indices α_{xg} vs α_{ox}. Designations are the same as in Fig. 13.